

Materials and Methods

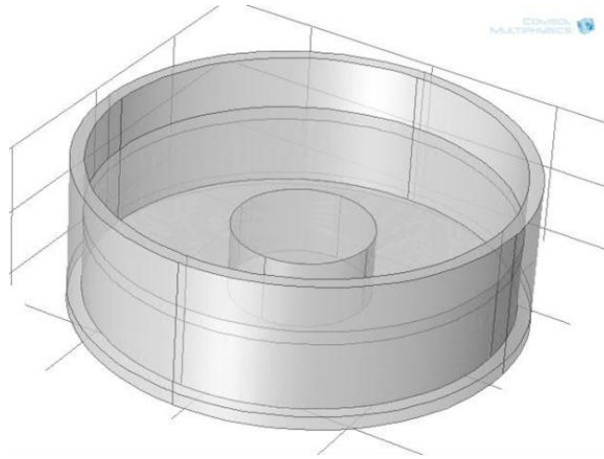


Figure 5.13: Geometry of the model developed with Comsol Multyphasic: a sample surrounded by water in a sample holder.

The physical and thermal properties necessary to solve the simulation were taken from the literature and from Comsol library: density (ρ), specific heat at constant pressure (c_p), thermal conductivity (k) and surface emissivity (ϵ) of the PMMA, the water and the sample-holder. To better simulate the transmission of heat, the modulus of heat transfer in solids [18] was applied to the sample and to the sample holder and the modulus of heat transfer in fluids was applied to the water. The initial condition of the model was 37°C taking into account the human body temperature. The boundary conditions of external environment were 23°C and the software evaluates the convection and irradiation contributions. The model took in input the value of specific power evaluated using the method presented in this work for P10 sample under a magnetic field of 22,5 mT. The value was 0,93 W/g (0,39 W). The exposed time was 15 minutes (900 s).

MATLAB[®] (MathWorks) was used to calculate and draw the diagrams of CEM_{43} vs. time.

The study performed by FEM was also compared with an experimental one on the same geometry and boundary condition. A P10 samples was put inside the large sample holder with 5 ml of water. All the system was heated up by the thermal power generated in inside the sample by a magnetic field of 22.5 mT with Egma 6 equipment at 220 kHz for 15 minutes.

The increase of the cement temperature was observed with an infrared-camera (V704 Flir-Fluka) focused on a sample surface visible point. The measure was performed in triplicate. The experimental set-up is shown in figures 5.14

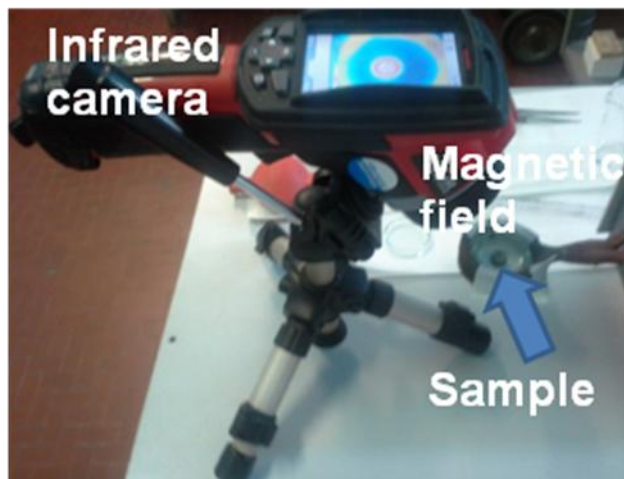


Figure 5.14: Experimental set-up for the detection of sample surface temperature with infrared-camera . P10 ,water and sample holder are placed in a magnetic field of 22.5 mT The sample is covered by 1 mm of distilled water

5.1.18. Production of antibacterial glass-ceramic

In order to impart antibacterial properties the original glass ceramic composition was modified by adding silver oxide or copper oxide. To include the antibacterial agent, different methods were investigated. .

5.1.18.1. Melting and quenching technique

The antibacterial SC45 glass ceramic was initially synthesized by **melting and quenching** techniques. The glass ceramic composition was modified with the addition of silver oxide, for one formulation (SC45 3Ag), and of copper oxide in the other (SC45 5Cu), in order to compare the antimicrobial behavior of these two different new glass-ceramics.

5.1.18.2. SC45 doped with Silver oxide

The Ag-doped glass ceramic composition is reported in table 5.3.

Fe_2O_3	FeO	SiO_2	CaO	Na_2O	P_2O_5	Ag_2O
30,3	13,7	24,1	13,2	12,4	3,2	3

Table 5.3: SC45-3Ag glass ceramic composition (%wt)

For the synthesis of SC45-3Ag, the %wt of Na_2O was lowered and 3% wt of Ag_2O was introduced. The amount of silver oxide was chosen on the base of literature [14].

Materials and Methods

The reactants for SC45 3Ag synthesis were: Na_2CO_3 (Sigma-Aldrich) with a purity $\geq 99,5\%$, CaCO_3 (Sigma-Aldrich) with a purity ≥ 99 , SiO_2 (Sigma-Aldrich) with a purity $\geq 99\%$, $\text{Ca}_3(\text{PO}_4)_2$ (Fluka) with a purity $\geq 96\%$, $\text{FeSO}_4 \cdot 7\text{H}_2\text{O}$ (Sigma-Aldrich) with a purity $\geq 99\%$ and Fe_2O_3 (Sigma-Aldrich) with a purity $\geq 99\%$ and AgCO_3 (Sigma-Aldrich) with a purity $\geq 99,5\%$. The reactants were weighted, mixed and homogenized with a mixing roller before melting.

The reactants were melted in a platinum crucible at 1550°C inside a high temperature furnace (Nabertherm- Carbolite 1800) for 25 min, using a heating rate of $10^\circ\text{C}/\text{min}$. The melt was cooled to room temperature in air by pouring in a brass mold, obtaining partially crystallized (glass-ceramic) bulk samples. Then, two different types of samples were obtained: one type was simply poured on the brass mold and the other was subjected to an annealing process in oven (Manfredi - 1200°C) at 600°C for 12h. This temperature guarantees none structural change in the glass ceramic because it is below the glass transition temperature (T_g) of SC45. The heat treatment was the aim to reduce the internal stress of the glass.

The bear, obtained after annealing treatment, was cut with a cutting machine in a slices with a thickness of about 1 mm (figure 5.15).



Figure 5.15: SC45-3Ag after annealing treatment at 600°C for 12 h

As it can be seen from Figure 5.16, the ferrimagnetic behaviour was still present after the silver doping.

Materials and Methods



Figure 5.16: Magnetic interaction between a magnet and SC45-3Ag after annealing treatment

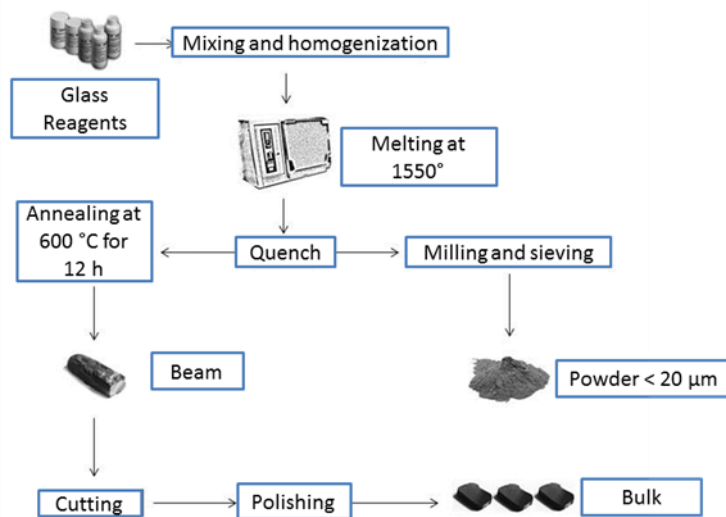


Figure 5. 17: A sum-up of the synthesis and the treatments of SC45-3Ag before the characterization

Figure 5. 17 shows the production process of SC45 3Ag. Samples were prepared both in powder form, after milling and sieving under 20 μm, and in a bulk form, after cutting and polishing, in order to investigate if the annealing process could have any influence on the structure and on the properties of SC45-3Ag.

An etching attack was performed on a bulk sample using a water acid solution (5% v/v). For this aim fluoridric (HF) and nitric acids (HNO₃) in 1:1 molar ratio were used. The slices of bulk were put in 20 ml of solution and left for 1 minute. After that they were washed with distillate water and prepared for FESEM investigation.

From now on, the samples identifications will be SC45 3Ag for powder samples and SC45-3Ag bulk for annealed samples.

5.1.18.3. Synthesis of SC45 doped with copper oxide

The SC45 5Cu composition is reported in table 5.4. The addition of copper (II) oxide implied a reduction in weight of calcium oxide of the SC45 composition. Taking inspiration from the literature, the amount of copper oxide was higher than the amount of silver oxide in SC45 3Ag, due to the lower antibacterial effect of copper in comparison to silver [15].

Fe ₂ O ₃	FeO	SiO ₂	CaO	Na ₂ O	P ₂ O ₅	CuO
31	14	24,7	8,5	13,5	3,3	5

Table 5.4: SC45-5u glass ceramic composition (%wt)

For the synthesis of SC45 5Cu the following reactants were used: Na₂CO₃ (Sigma-Aldrich) with a purity ≥99,5%, CaCO₃ (Sigma-Aldrich) with a purity ≥99, SiO₂ (Sigma-Aldrich) with a purity ≥99%, Ca₃(PO₄)₂ (Fluka) with a purity ≥96%, FeSO₄*7H₂O (Sigma-Aldrich) with a purity ≥99% and Fe₂O₃ (Sigma-Aldrich) with a purity ≥99% and CuO (Fluka) with a purity ≥ 99%.

The reactants were weighted, mixed and homogenized with a mixing roller before melting.

The reactants were melted in a platinum crucible at 1550°C inside a high temperature furnace (Nabertherm- Carbolite 1800) for 25 min, using a heating rate of 10°C/min. The melt was cooled to room temperature in air by pouring in a brass mold, obtaining partially crystallized (glass-ceramic) bulk samples. As mention before for the SC45 3Ag samples, also for SC45 5Cu some samples were only poured on the brass mould while others were subjected to an annealing process in oven (Manfredi -1200°C) at 600 °C for 12h, for internal stress relaxations. The sample identification for these glass ceramic will be SC45 5Cu and SC45-5Cu bulk, respectively.

5.1.18.4. Calorimetric test

Calorimetric tests were performed for the evaluation of the heat generation of glass ceramic doped with silver and copper. The method was the same used for magnetic cements. The applied magnetic field was fixed at 22,6 mT as the frequency at 220 kHz. The temperature increase was recorded after 6 minutes, when the magnetic field was off, with a digital thermocouple. At time

zero the sample temperature were equal to room temperature. The mass of the sample introduced into the test tube was 0,5 g. The analyzed specimens were in a powder form (bulk samples were grinded and sieved) with a controlled particle size dimension under 20 μm . The initial temperature was about 21 °C and ΔT was evaluated between initial and final temperature.

5.1.18.4.1. Molten Salt ion Exchange

The process of ion exchange in a glass takes place when ions (generally monovalents) of a surface layer of a glass are replaced by ions of a different species, present in an external solution.

The ion exchange is a process of thermal diffusion, realized by immersion of the glass in a molten salt bath containing the ions to be introduced into the glass network as modifier agents.

This technique was applied to the SC45 glass-ceramic, by the use of a silica crucible with a purity > 99%, in which a thin layer of glass-ceramic (SC45) particles was interposed between two layers of salts previously mixed; the crucible was inserted into an alumina cup and placed in a oven (Manfredi-1200°C).

The melting temperature of the treatment was chosen taking into account the single melting temperatures of the salts. The ion exchange in molten salt was performed at 380°C with an heating rate of 10°C/min to ensure salts fusion without any change in glass structure

The heat treatment lasted 30 min since the oven reached 380°C. Then the crucible was removed from the oven, cooling at room temperature and the material is quenched on a brass plate (figure 5.18).

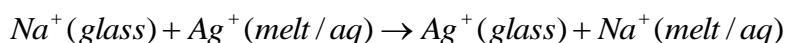
A washing process was necessary to remove salts that can accumulate on the SC45 particles and interfere during the further characterizations; therefore a series of washing treatments, with distilled water in ultrasound equipment, were performed, favouring the precipitation of SC45 powders and dissolution of salts. The washing treatments in distillate water and ultrasound were repeated for three times for each exchanged powder. At the end of washing treatment, the water was aspirated with a pipette, leaving on bottom of the container only the precipitated glass ceramic powders. Finally the powders were filtered and they were dried in an oven at 60° overnight.

Materials and Methods

The molten salt ion exchange process was developed in the same way both for SC45 doped with Silver and with SC45 doped with copper. The difference between these two processes regards only the used molten salt .

5.1.18.4.1.1. SC45 doped with silver nitrate

The following chemical reaction clarifies the ion exchange process:



The molten salts used for the treatment were sodium nitrate ($NaNO_3$) and silver nitrate ($AgNO_3$).

Sodium Nitrate (Sigma Aldrich) has a melting temperature of 310 °C while silver nitrate (Sigma Aldrich) melts at 210 °C.

Three ion exchange were developed for three different molar concentration of silver. This choice permitted the investigation of the effect of silver on glass ceramic properties as already reported in [16].

Sample identification	$NaNO_3/AgNO_3$ mol/mol	Silver content
Ag 20	20	High
Ag 200	200	Medium
Ag 2000	2000	Low

Table 5.5: Synthesis of SC45 doped with different molar concentration of $AgNO_3$

In table 5.5 the sample descriptions of doped SC45 with different molar concentration of silver are reported.



Figure 7.18: SC45 doped with ion silver after ion exchange with molten salt. The samples SC45 Ag20, SC45 ,Ag200, SC45 Ag2000) were quenched on a plate and then put in water for salt dissolution.

5.1.18.4.1.2. SC45 doped with copper nitrate

The molten salts used for the treatment were sodium nitrate (NaNO_3) and copper nitrate ($\text{Cu}(\text{NO}_3)_2 \cdot 3\text{H}_2\text{O}$).

Sodium Nitrate (Sigma Aldrich) has a melting temperature of 310 °C while copper nitrate (Sigma Aldrich) melts at 114 °C.

The doping process on SC45 was performed for three different molar concentration of copper as for silver. This choice permitted the investigation of the effect of copper on glass ceramic properties [16].

Sample identification	$\text{NaNO}_3/\text{Cu}(\text{NO}_3)_2$ mol/mol	Copper content
Cu 20	20	High
Cu 200	200	Medium
Cu 2000	2000	Low

Table 5.6: SC45 doped with different molar concentration of $\text{Cu}(\text{NO}_3)_2$

In table 5.6 the sample descriptions of SC45 doped with copper in different molar concentrations are reported.

5.1.18.4.2. Calorimetric test

Calorimetric test was performed using an alternate magnetic field with the aim of detecting the increase in temperature of a known volume of water containing samples of defined size, weight and morphology. The test was developed using a magnetic induction furnace Egma 6 (Felmi S.r.l) generating a magnetic field intensity of 22,5 mT at fixed working frequency of 220 kHz. 0.5 g of powder samples with a controlled particles size under 20 μm were immersed in 16 ml of distilled water and the initial temperature (T_{in}) was measured with a thermocouple. Then, the tube containing the samples was positioned in the middle of the coils of the inductor with a high of 106 mm. The change of inductor coil takes into account the fact that the samples are powder. The convective motion of the water inside the test tube influenced the diffusion of the particles. A magnetic induction was applied and the final temperature (T_{fin}) was measured after 2, 4, 6, 8, 10

Materials and Methods

and 12 min. After each measurement samples were cooled in air at room temperature. The same test was repeated three times for each powder formulation to minimize the data scattering.

5.1.18.4.3. Antibacterial test

The antibacterial inhibition halo test was carried out according to the standard [18], using a *Staphylococcus aureus* standard strain (ATCC 29213).

The inhibition halo test allows the samples placement in contact with an agar plate (Mueller Hinton agar) uniformly covered with a bacterial broth, previously prepared with a standard procedure, and their overnight incubation at 35°C.

The procedure for the Mueller Hinton agar realization foresees the preparation of a standard 0.5 McFarland (containing approximately $(1-2) \times 10^8$ CFU/ml) by dissolving some bacterial colonies (previously cultured on Blood Agar plate, figure 5.19) in a physiological solution. The McFarland index is a turbidity measurement and it was evaluated by optical instrument—Phoenix Spec BD McFarland).

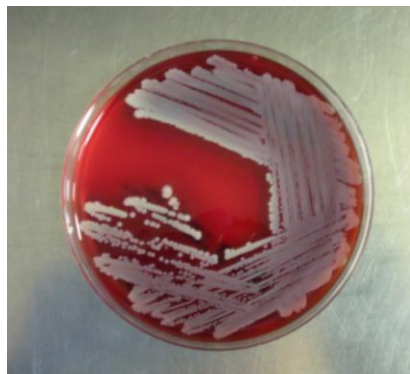


Figure 5.19: bacterial colonies spread on the agar blood plate

It was necessary the preparation of a solution of 0.5 McFarland of the bacterial strain to be tested. Subsequently an aliquot of this suspension was spread on Mueller Hinton agar plates using a cotton buds by carrying out three dense passages with different orientation (45°), as described in figure 5.20.

Materials and Methods

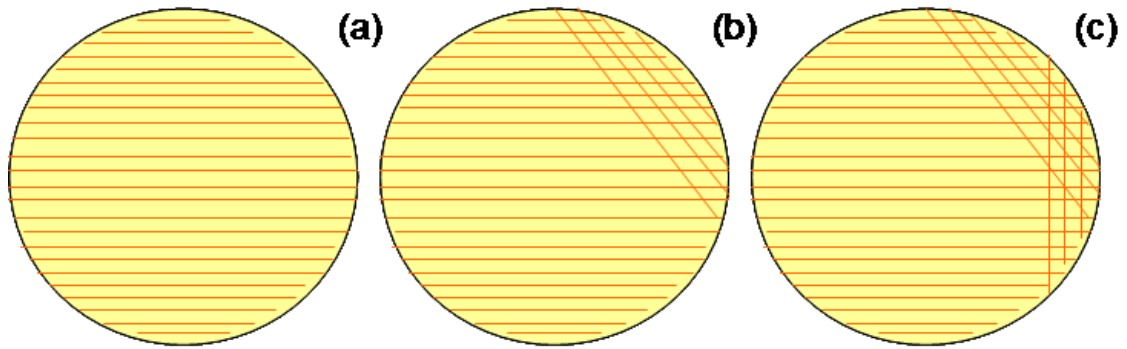


Figure 5.20: Preparation of Mueller Hinton plate for antibacterial test.

Afterwards, as mentioned before, samples were placed in contact with agar and incubated 24 h at 35 °C in the agar plate; at the end of incubation the inhibition halo formation was observed and measured (see figure 5.21).

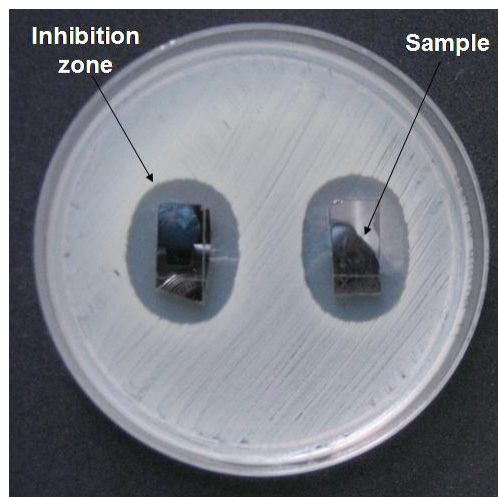


Figure 5.21: Example of inhibition halo after antibacterial test

For this characterization the samples were produced using 200 mg of SC45 and doped SC45 powders uniaxially pressed at 4 tons for 10 seconds in order to prepare disks of a diameter of 1 cm and a thickness of 0,5 mm.

5.1.18.4.4. Bioactivity tests

Bioactivity test was carried out on the three compositions of the glass-ceramic doped with silver and copper using the ion exchange molten salt process, compared with control (SC45), after three and four weeks of immersion in SBF.

For each time point two samples for type (sixteen samples in total) were prepared; each sample, was composed by 100 mg of powder that was soaked in 100 ml of SBF and moved with an orbital

Materials and Methods

shaker, programmed to maintain a temperature of 37 °C and a rotation of 150 rpm for the duration of the entire test. No refresh was performed [19]. By using a digital pH meter, the pH of the SBF was measured every two days, until the date of extraction of the sample. After three and four weeks, powders were extracted from the solution by filtering. Finally the powder were placed in incubator for one day at 37 ° C to dry them.

5.2. Reference

1. Larry LL, June Wilson H, An introduction to bioceramics. Singapore: Word Scientific, 1993.
2. Bretcanu O, Verne' E, Coisson M, Tiberto P, Allia P, Temperature effect on the magnetic properties of the coprecipitation derived ferrimagnetic glass-ceramics. *J Magn Magn Mater* 2006; 300: 412–417.
3. Bretcanu O, Spriano S, Brovarone VC, Vernè E, Synthesis and characterization of coprecipitation-derived ferrimagnetic glass-ceramic. *J Mater Sci* 2006; 41: 1029–1037.
4. Bretcanu O, Ferraris S, Miola M, Vernè E, *Adv in Bioc and Biotech: Cer Trans*. New York: Wiley & Sons ;2012:139–144.
5. Bretcanu O, Spriano S, Verne` E, Coisson M, Tiberto P, Allia P, The influence of crystallized Fe_3O_4 on the magnetic properties of coprecipitation-derived ferrimagnetic glass-ceramic. *Acta Biomater* 2005; 1: 421–429.
6. Vernè E, Miola M, Ferraris S, Bretcanu O, Surface activation of a ferrimagnetic glass-ceramic for antineoplastic drugs grafting. *Adv Eng Mater* 2010; 12: B309–B319.
7. Bretcanu O, Verne' E, Coisson M, Tiberto P, Allia P, Magnetic properties of the ferrimagnetic glass-ceramics for hyperthermia. *J Magn Magn Mater* 2006; 305: 529–533.
8. Incropera FP , DeWitt DP, *Fundamentals of heat and mass transfer*. New York: John Wiley & Sons, 1996.
9. *Lezioni di Fisica I : l'impedenza*
10. Halliday D, Resnick R, Walker J, *Fondamenti di Fisica Meccanica e Termologia*, Casa editrice Ambrosiana 2006: 536.
11. International standard ISO 5833:2002 (E) Implants for surgery — Acrylic resin cements.
12. Petrucci G , *Proprietà dei materiali e prove meccaniche*.
13. William K, Szaroletta NL ,Purdue D, *Four Point Bending: A New Look*.
14. Sharma K, Meena SS, Saxena S, Yusuf SM, Srinivasan A, Kothiyal GP, Structural and magnetic properties of glass-ceramics containing silver and iron oxide, *Mater Chem and Phys* 2012; 133: 144–150.
15. AM Abdel-Hameed, Marzouk MA, Abdel-Ghany AE, Magnetic properties of nanoparticles glass-ceramic rich with copper ions, *J of Non-Cry Sol* 2011; 357: 3888–3896.

Materials and Methods

16. Di Nunzio S, Vitale Brovarone C, Spriano S, Milanese D, Vernè E, Bergo V, Maina G, Spinelli P, Silver containing bioactive glasses prepared by molten salt ion-exchange, *J of Eur Ceram Soc* 2004; 24: 2935-2942.
17. Kokubo T, Takadama H, How useful is SBF in predicting in vivo bone bioactivity? *Biomater*; 2006; 27: 2907-2915.
18. NCCLS M2-A9. Performance Standards for Antimicrobial Disk Susceptibility Tests Approved Standard, 9th Edn, NCCLS, Villanova, PA, USA 2003.
19. Perdomo MM, Meille S, Chenal JM, Pacard E, Chevalier J, Bioactivity modulation of Bioglass® powder by thermal treatment , *J of Eur Ceram Soc* 2012; 32: 2765-2775.

Chapter 6

Results and Discussion

Composite bone cement characterization

6.1 Characterization of glass ceramic

6.1.1 XRD and SEM EDS analysis

The XRD pattern of SC45 glass ceramic is shown in SC45 X-ray diffraction pattern in figure 6.1. In the pattern the peaks of magnetite (Fe_3O_4) (ref. code 01-076-1849) can be observed, the main crystalline phase produced during cooling of the melt, and the amorphous halo, characteristic of the residual glassy phase between 25 and 35 2θ are reported in [1]. A small amount of hematite is also observed even if it is negligible with respect to the main crystalline phase.

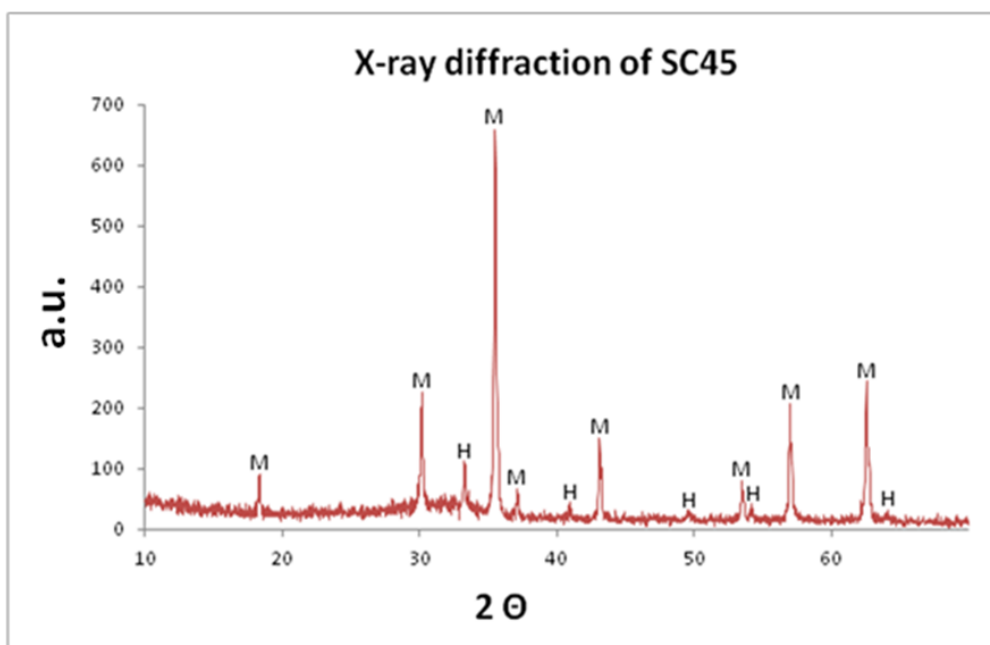


Figure 6.1: SC45 X-ray diffraction pattern. M indicates Magnetite and H hematite

Magnetite crystals are formed during cooling of the melt, without any successive crystallization treatment and they are uniformly distributed in the amorphous matrix, as already observed and reported in a previous paper [1]. The SEM-EDS analyses of SC45 powders (figure 6.2) confirm the presence of magnetite crystals embedded inside a residual amorphous matrix. The crystalline phase presents an octahedral shape, a columnar distribution and is well dispersed throughout the glass matrix.

Results and Discussion Composite bone cement characterization

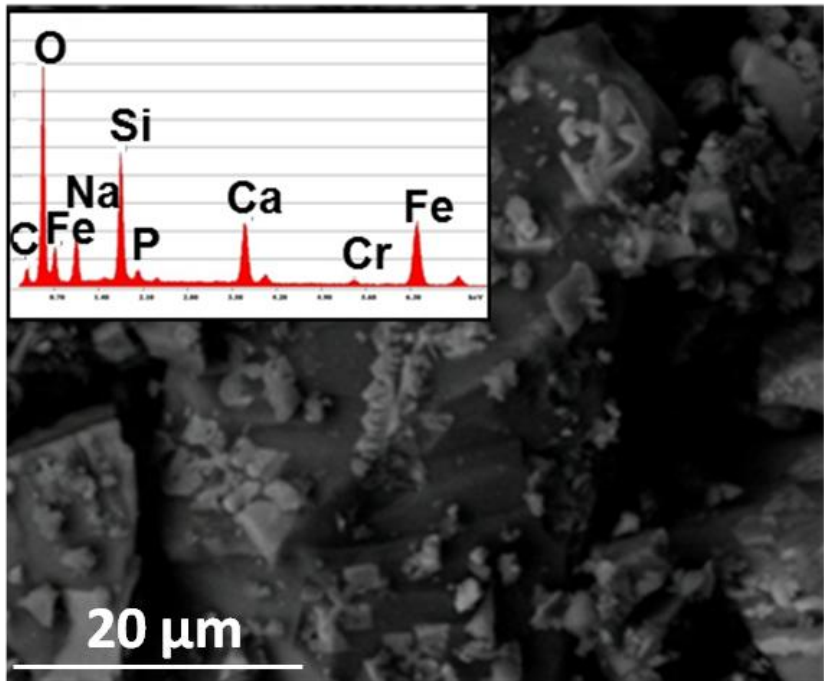


Figure 6.2: Morphological and compositional evaluation of SC45

The EDS spectrum confirms the presence of the peaks corresponding to the elements of the SC45 composition (Si, Na, Ca, P, Fe and O). The Cr peak is due to the sample metallization necessary for the SEM analysis.

The evaluations of the magnetite amount using the X-Ray Diffraction method is shown in figure 6.3.

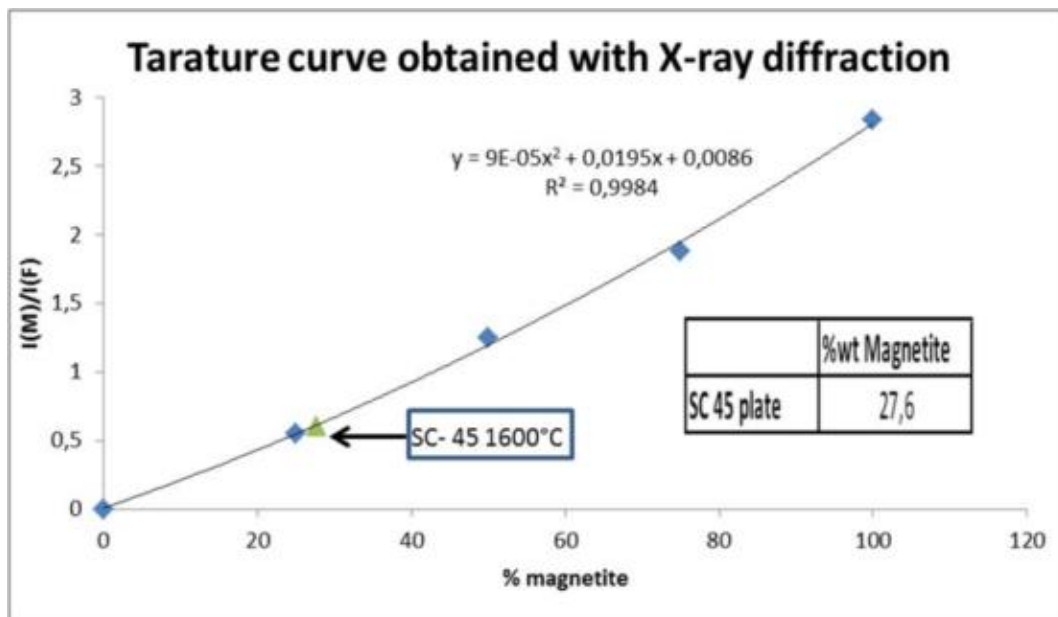


Figure 6.3: Evaluation of % wt. of magnetite in the glass ceramic with XRD methods

The results of the X-ray diffraction procedure show 27.6 %wt. of magnetite.

6.1.2 Experimental method for the evaluation of magnetite into the SC45 glass ceramic

The quantification of the amount of magnetite inside the glass-ceramic is also evaluated with eq.1 (see Material and Method chapter) estimating the saturation magnetization values from the hysteresis cycles up to 800 kA/m of pure magnetite and of SC45.

An amount of 28.6 % of magnetic phase is obtained, that is almost the same value that was found out in the previous XRD analysis (figure 6.4). Then, it is estimated with two different methods that iron is not completely coordinated in the magnetite crystals but is partially embedded in the glass network.

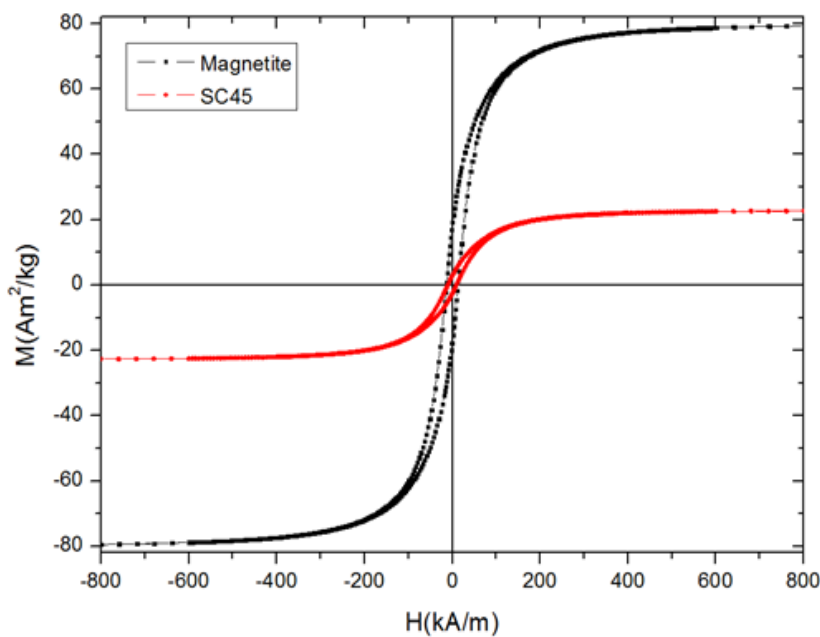


Figure 6.4: Hysteresis loops of pure magnetite and SC45 for the quantification of %wt of Fe₃O₄ in the glass.

The calculated amount of magnetite differs from the theoretical amount. The iron, in the theory of glass formation, behaves as an intermediate constituent. In fact it can appear as a glass former, taking the position of silicon in the network of the glass, or as a modifier breaking the bonds of the bridging oxygen between tetrahedral silica. The presence of iron ion in the glass matrix does not produce a magnetic contribution, which is only produced by magnetite that generates heat under a stimulation of an alternate magnetic field.

6.1.3 Glass ceramic bulk: elemental mapping

SEM-EDS elemental mapping of a SC45 synthesized in bulk form is shown in figure 6.5. The EDS elemental mapping is based on the identification of different elements using different colors in order to observe their distribution inside the material. As can be seen the elements Si, Ca, Na are confined in the amorphous matrix and oxygen, as expected, is dispersed both in the magnetite crystals and in the glassy matrix. Fe is present not only in the magnetite crystals, but also in the amorphous matrix, confirming the hypothesis that not all the iron atoms are involved in the magnetite crystal formation. Figure 6.5f shows a uniformity red color both on magnetite crystals and on the glass matrix.

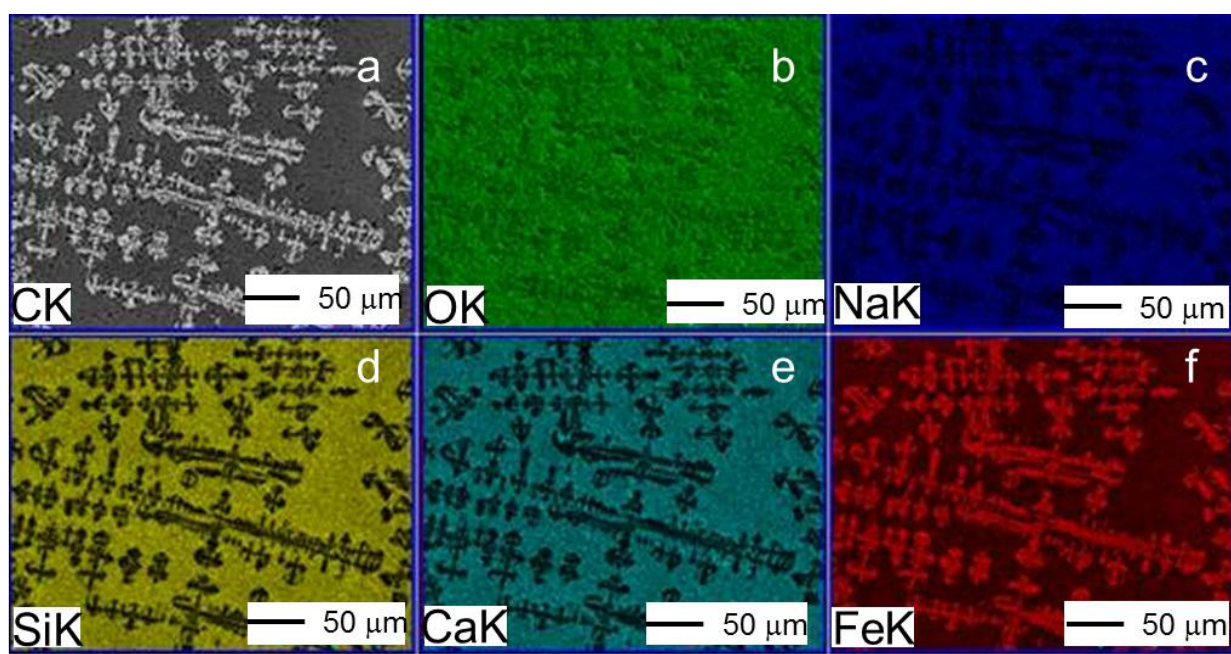


Figure 6.5: SEM-EDS elemental mapping of a SC45 bulk sample. SEM image of SC 45 glass-ceramic (a) , oxygen (b) , sodium (c) , silicon (d) , calcium (e) and iron (f) distribution.

6.2. Composite bone cement characterizations

6.2.1. Morphological and compositional characterization

SEM-EDS analyses of P10, P15 and P20 samples were performed in order to investigate the distribution of the SC45 powders inside the PMMA matrix. Figure 6.6 shows the surfaces of the composite bone cements captured in backscattering method with SEM microscope. The presence of the SC45 powders (identified with arrows in the images) and the zirconia (the radio-opaque agent identified with circles in the images, already present into the commercial formulation) are

Results and Discussion Composite bone cement characterization

well dispersed among the PMMA spheres. The PMMA powders have a spherical shape with a diameter between 10-20 μm and 70-80 μm , ZrO_2 is present in the form of aggregates with maximum dimension of about 20-30 μm and, as expected, the SC45 powders have a grain size below 20 μm .

The compositional analyses make evident the presence of the characteristic peaks of the glass-ceramic and of the zirconia, together with the PMMA peaks (C, O) and Cr peak due to the samples metallization for the perform of scanning electron microscopy. The total amount of zirconia is 10% .

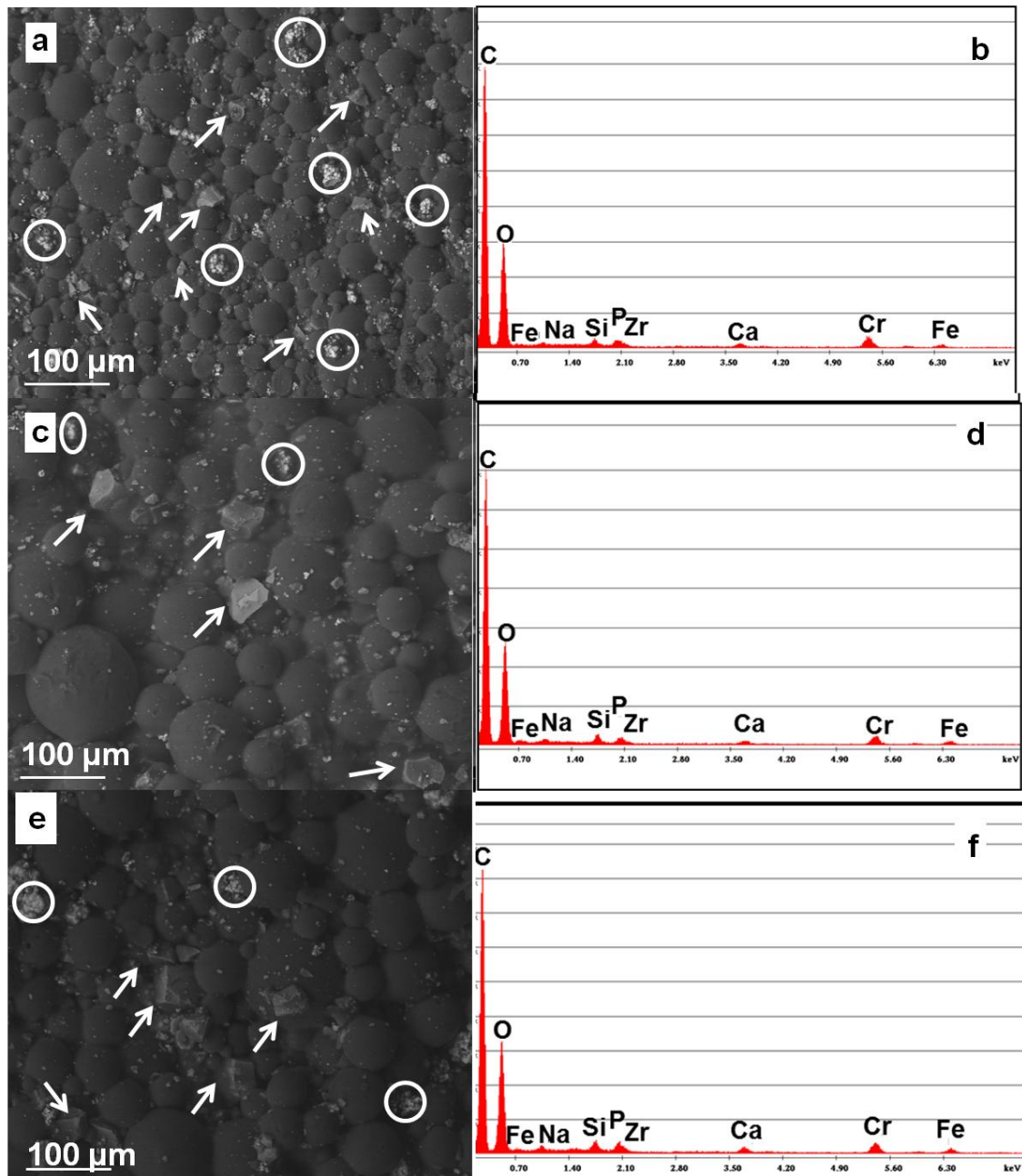


Figure 6.6: Morphological and compositional analysis of magnetic bone cement surfaces: (a-b) P10, (c-d) P15, (e-f) P20.

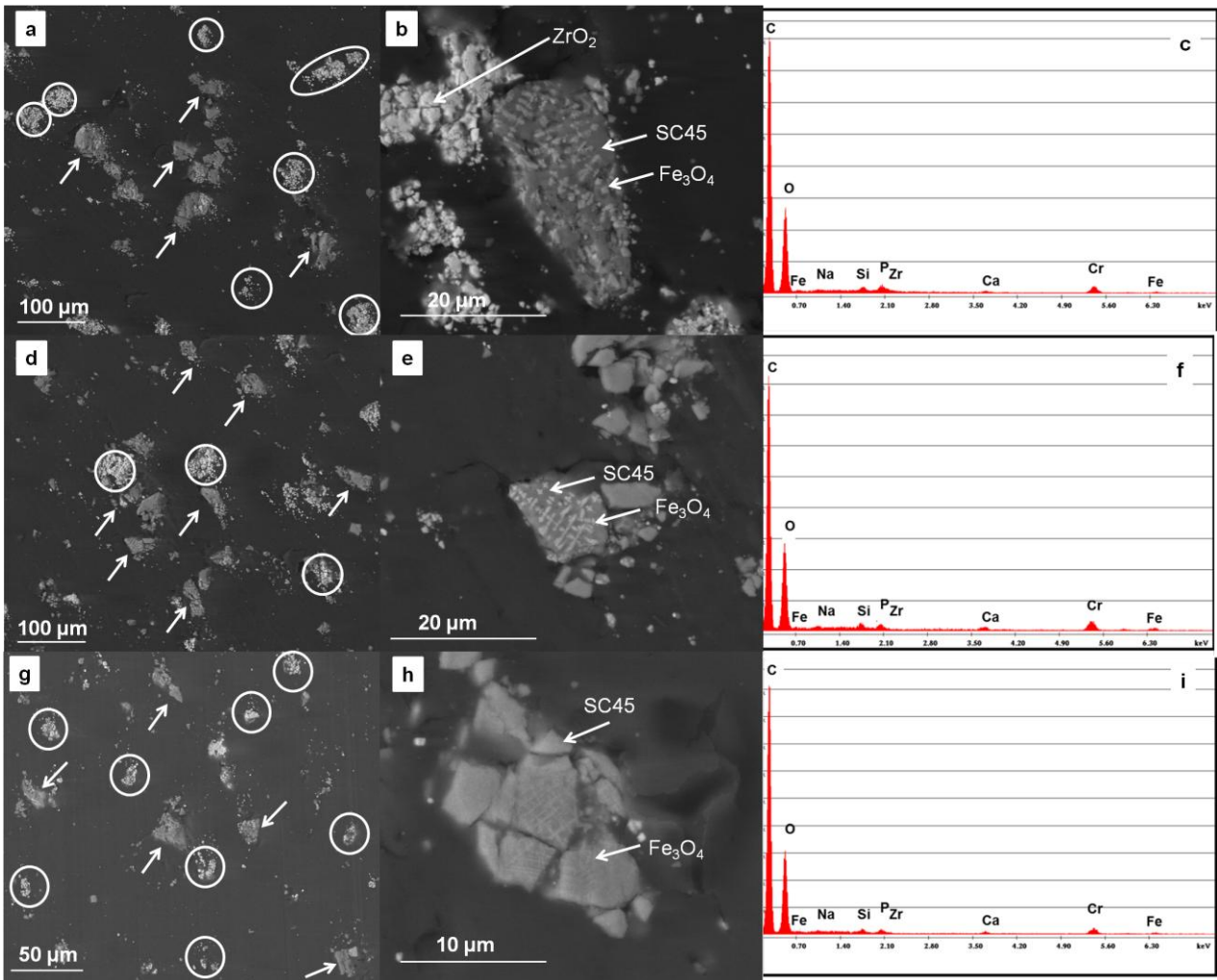


Figure 6.7: Morphological and compositional analysis of magnetic bone cement surfaces: (a-b-c) P10, (d-e-f) P15, (g-h-i) P20.

Figure 6.7 shows the SEM-EDS analyses of samples cross sections. The presence of SC45 powders and ZrO_2 aggregates well dispersed in the PMMA matrix can be noticed. The figure also shows some magnifications of the SC45 powders embedded in the PMMA, in which the magnetite crystals are well visible. The crystals have sub micrometric dimension and they are included in the glass amorphous phase.

This first characterization (figures 6.7 a, d and g) has the aim of making evidence the homogeneous distribution of glass both on the surface and inside of the samples. This permitted to deduce that the manual mixing method for the cements synthesis does not create any particle agglomeration, as shown clearly in the following test.

6.2.2. Micro CT reconstruction

The tomography images allow to reconstruct a 3D structure of sample in order to distinguish the different phases, which correspond to dissimilar material density. Figure 6.8a and 6.8b show respectively a volume of the commercial bone cement and the P20 composite cement. The red color shows the polymeric matrix, the blue one evidences the dispersed phase inside it, while the black is the porosity. The two images are taken at the same magnification and with the same orientation for comparative purposes. As expected, in figure 6.8a (commercial cement) the dispersed phase is less than in figure 6.8b (P20), since the commercial cement contains only zirconia (10%wt.) as inorganic phase, while P20 contains also 20%wt. of ferrimagnetic glass-ceramic. Both images evidence a homogenous distribution of the particles without the presence of large agglomerate, as also confirmed by SEM images.

Figure 6.8c and figure 6.8d represent a sample volume cut with the coronal (red boundary line), the sagittal (green boundary line) and transverse (blue boundary line) planes. In these pictures the whole volume of the composite material (PMMA and inorganic phases) was taken into account, so they allow the identification of the samples porosity (black holes): the commercial sample (figure 6.8c) appeared less porous than the P20 sample (figure 6.8d). The presence of a not negligible porosity in the composite cements could affect the mechanical properties as will be discussed in paragraphs 6.2.11.1, 6.2.11.2.

It was chosen the 3D reconstruction of these two samples (commercial cement and composite with the highest SC45 amount) in order to show much better the differences.

Results and Discussion Composite bone cement characterization

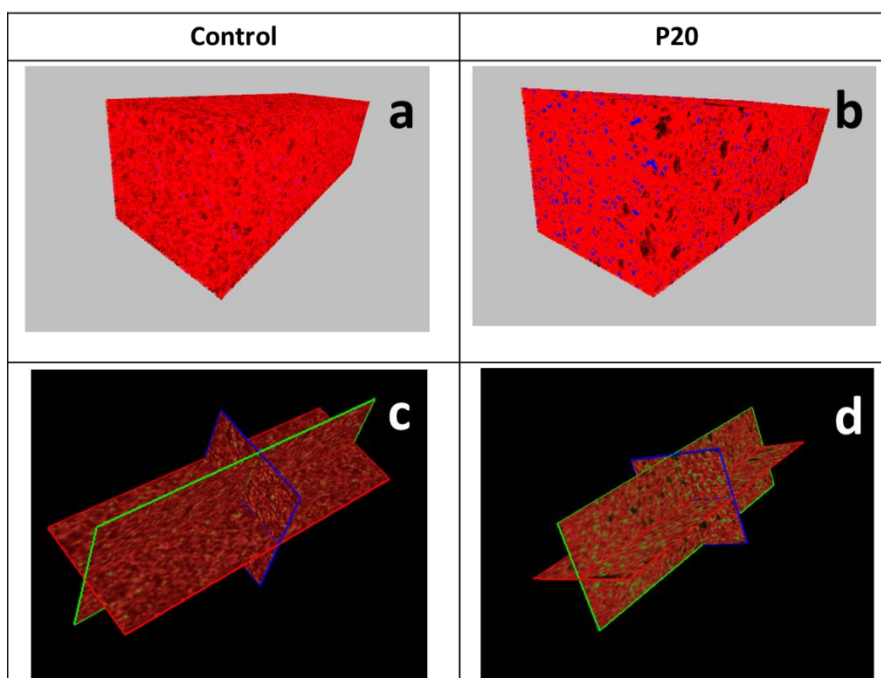


Figure 6.8 : Two different view of 3D reconstruction of control and P20 samples: (a) , (c) represent the control sample while (b),(d) P20 sample.

6.2.3. Setting time evaluation

Sample name	T max of polymerization [°C]	Acceptance requirements ISO 5833	Average setting time [mm:ss]	Acceptance requirements ISO 5833
Palamed tq	48 ± 4	90 ° C	12:29 ± 01:00	3-15 min
P10	49 ± 3		11:51 ± 01:00	
P15	49 ± 2		12:00 ± 01:00	
P20	49 ± 2		12:15 ± 01:00	

Table 6.1: Setting time and maximum temperature polymerization of the composite bone cements in comparison with a control PMMA

Table 6.1 reports the setting time and maximum polymerization temperature of all tested formulation. The values are in agreement with the standard ISO 5833 and the addition of SC45 doesn't change the setting time and polymerization temperature respect to the control.

The polymerization temperature is much lower than the maximum accepted values. As described in the SEM analysis of the composite surface, the maximum particles size of PMMA beads are

Results and Discussion Composite bone cement characterization

between 70-100 μm . Pascual et al. reported, in figure 6.9, an inverse proportionality between the mean particle sizes of PMMA powder and the maximum polymerization temperature [5]. The obtained polymerization temperature are in agreement with the size.

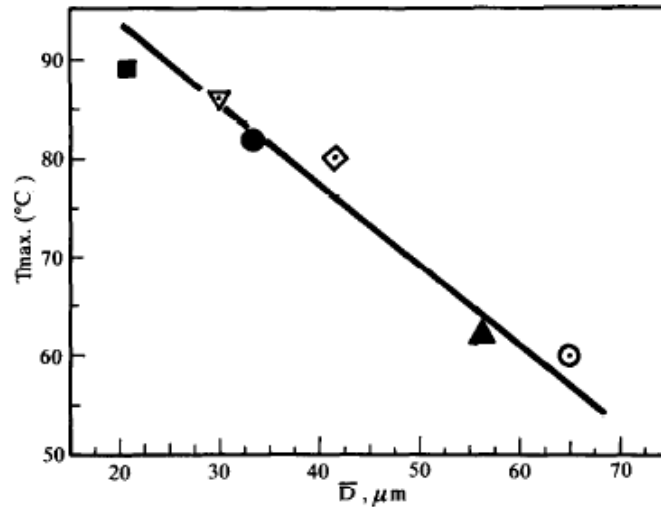


Figure 6.9: Correlation between mean PMMA particle size and maximum polymerization temperature[5]

6.2.4. Hysteresis cycle measurements

Figure 6.10 evidences a typical behavior of a ferrimagnetic material where all the composite samples reached the saturation magnetizations. The energy loss per mass (unit) produced by the hysteresis cycle is proportional to the heat that can be generated in the phenomena of hysteresis loss. High frequency looping of the magnetic field implies a path "reduced" of the hysteresis loop, and then energy dissipated per cycle results much less than the maximum available.

Results and Discussion Composite bone cement characterization

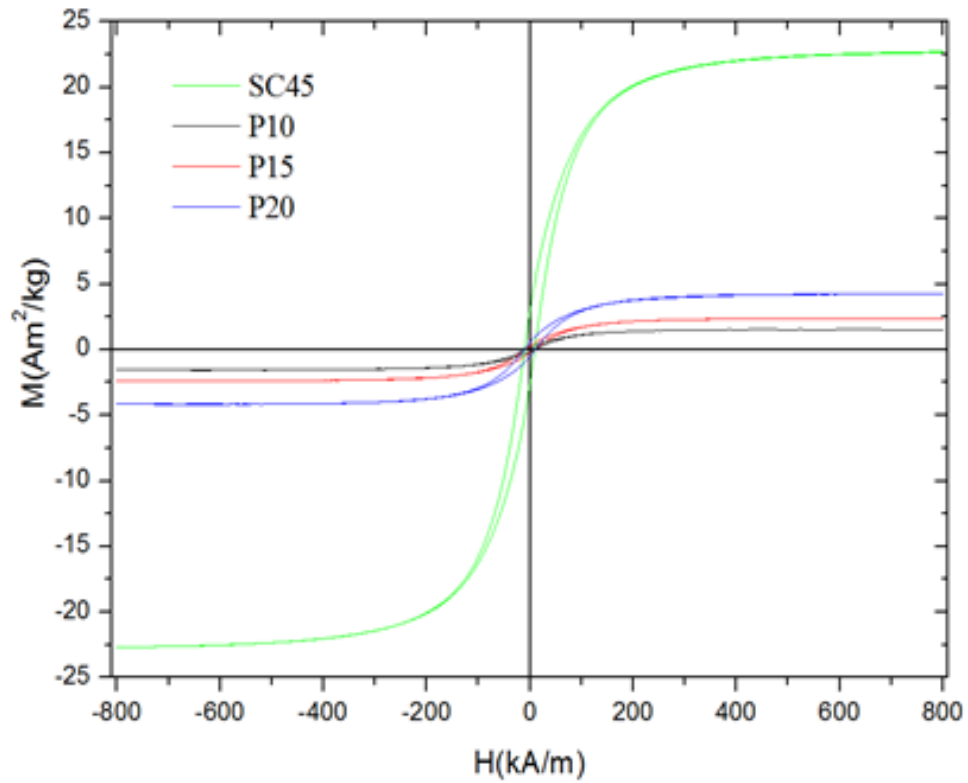


Figure 6.10: Hysteresis loops of the glass ceramic SC45 and P10, P15, P20 composite up to 800 kA/m

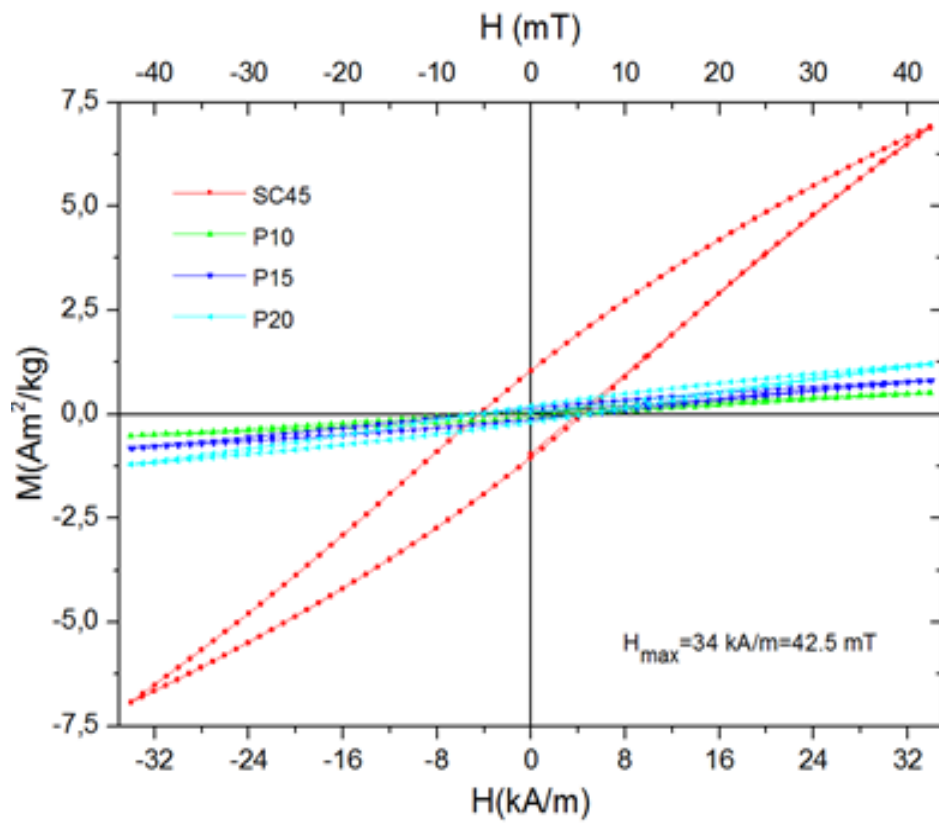


Figure 6.11: Hysteresis cycle of SC45, P10, P15, P20 composite up to 34 kA/m

Results and Discussion Composite bone cement characterization

In figure 6.11 are shown the hysteresis cycles at 34 kA/m for all the composite . As expected the hysteresis loops decreases , decreasing the external magnetic field but the highest hysteresis area was also obtained for SC45. The hysteresis cycles are not completely closed but the proportionality between the amount of the SC45 in the polymer matrix and the magnetization is respected.

Sample	Remanence magnetization M_r (A*m ² /Kg)	Coercitive force H_c (kA/m)	Saturation magnetization M_s (A*m ² /kg)	Hysteresis energy loss at ± 800 kA/m (J/kg)	Hysteresis energy loss at ± 34 kA/m (J/kg)
SC45	2,9	10	22,7	0,70	0,1
P10	0,18	9,7	1,6	0,05	0,007
P15	0,27	9,75	2,5	0,08	0,012
P20	0,53	9,8	4,2	0,12	0,019

Table 6.2: Magnetic parameters evaluated from hysteresis cycles of SC45 , P10,P15,P20 composite

In Table 6.2 remanence magnetization (M_r), coercive force (H_c), saturation magnetization (M_s) and hysteresis energy loss at ± 800 kA/m and ± 34 kA/m are reported. The saturation magnetization increases from P10 to P20. It varies from 1,6 to 4,2 A*m²/kg, while the coercive force does not change. This result confirms the presence of the same type of magnetite in all bone cements. Increasing the quantity of the glass ceramic inside the polymer matrix , M_r and M_s value increase and they depend on how much magnetic phase is inside the polymer. The SC45 sample has the highest value of M_s and it can be consider the material reference for the composite. Also the hysteresis energy loss present the same trend, by increasing the amount of magnetite into the cement the cycle expands.

6.2.5. Calorimetric results

6.2.5.1. Preliminary results

The first calorimetric characterization on the composite bone cement produces the following results. In figure 6.12 it is represented the increase of temperature during the period of heating generated by the alternative magnetic field. For all the formulation (P10, P15 and P20) ΔT increases while, for the control, there is no increase of temperature. This is an expected result because the heat generation depends on the amount of magnetite inside the polymer. Moreover the control test point out that eddy current generates from the polymer and from the distilled water are negligible in respect to the hysteresis losses.

Results and Discussion Composite bone cement characterization

Magnetite has an high resistivity, a low conductivity an even the contribution of eddy current are very low with high hysteresis energy, making the generation of heat proportional to the applied frequency and related only to hysteresis loss. . Di Gerlando et al.[6] report a typical values of resistivity for a common ferrite: $\rho_{\text{fer}} \approx 10^{10} \mu\Omega\text{m}$. The higher is the resistivity of the material, the smaller will be the intensity of the eddy currents and therefore the lower will be the dissipation of electrical energy into heat. These properties are very important for magnetic hyperthermia application because they permit controllability and reproducibility of the material.

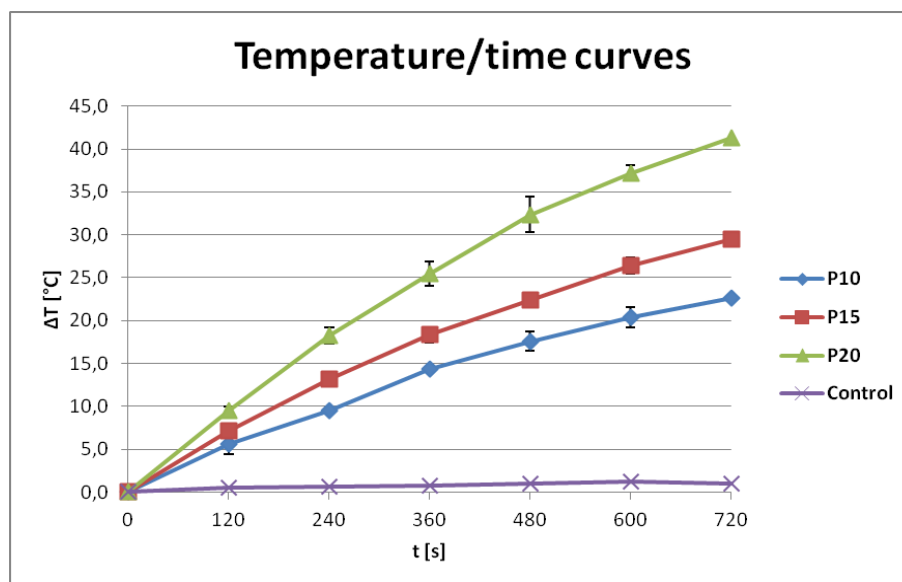


Figure 6.12: Calorimetric measurements with constant $B=48$ mT at 220 kHz for 720 s

The parabolic trend of all curves demonstrate a non-linear behavior due to the effect of thermal dispersions, which in this test are not evaluated. But, as it can be seen from the curves, at elevated temperature variations the effect of dispersions is not negligible. Increasing from 10 to 20 % wt of SC45 into the polymer, the amount of magnetite increases, causing an rise increase of water temperature in which the samples are put at a fixed magnetic field. This phenomenon is more marked in the curve with P20 as the reached temperatures are higher, and consequently also the dispersions. Theoretically, the temperature variation should increase slowly with time and increase up to an asymptotic value, when the generated heat is equal to dissipated one. This aspect is an advantage for the future *in vivo* hyperthermia therapies because the final steady state value causes self-limiting of temperature increase.

For the calorimetric characterization of these materials it is also important the quantification of specific power losses, which represents the value of total generated energy divided by a specific amount of material. The expression represents a normalized value respect to a mass of material.

Results and Discussion Composite bone cement characterization

In these preliminary evaluations the specific power losses were calculated with the following formula [8]:

$$P = \frac{c_w * m_w * \Delta T}{t * m}$$

$$\Delta T = T_f - T_i$$

Where

P = specific power loss (W/g)

Q = $c_w * m_w * \Delta T$, heat absorbed by water (J)

t = exposure time (s)

m=sample's mass (g)

m_w =water's mass (g)

c_w =water's specific heat (J/g °C)

ΔT the temperature variation (°C)

T_i = initial temperature of water (°C)

T_f = final temperature of water (°C)

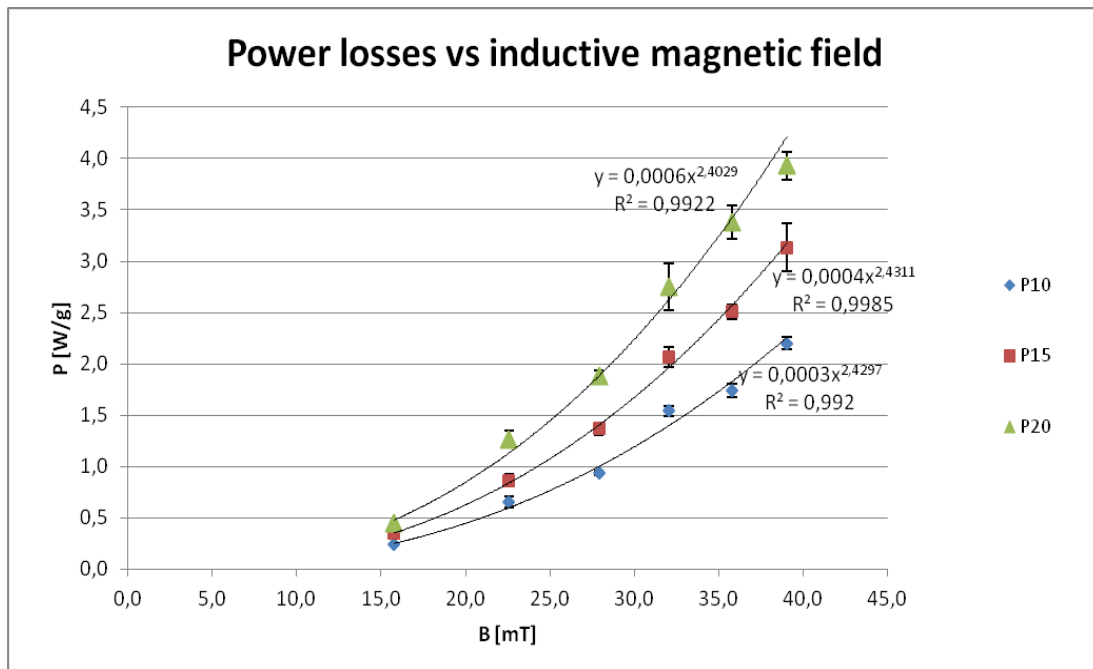


Figure 6.13 : Graphic of magnetic induction respect to thermal power loss measured at f= 200 kHz and t=240 s

The power generation evaluated in respect to magnetic field is reported in figure 6.13. Due to the fact that the specific power losses depend from the amount of magnetite inside the composite and by the applied magnetic field, it has been possible to use Steinmetz's equation for the

Results and Discussion Composite bone cement characterization

evaluation of magnetic losses as the best fitting function of data [7]. The formula expresses a linear correlation among the power losses, the induction magnetic field and the working frequency.

$$P_s = c * B^n * f$$

Where

P_s = specific power loss (W/g)

c = constant depending on material magnetic properties and magnetite concentration

f = frequency of magnetic field (constant in our test) (Hz)

B = magnetic induction (T)

$n = 2,4$ as the best fit of experimental data.

As you can see linear regression coefficients are very close to 1 for all formulations.

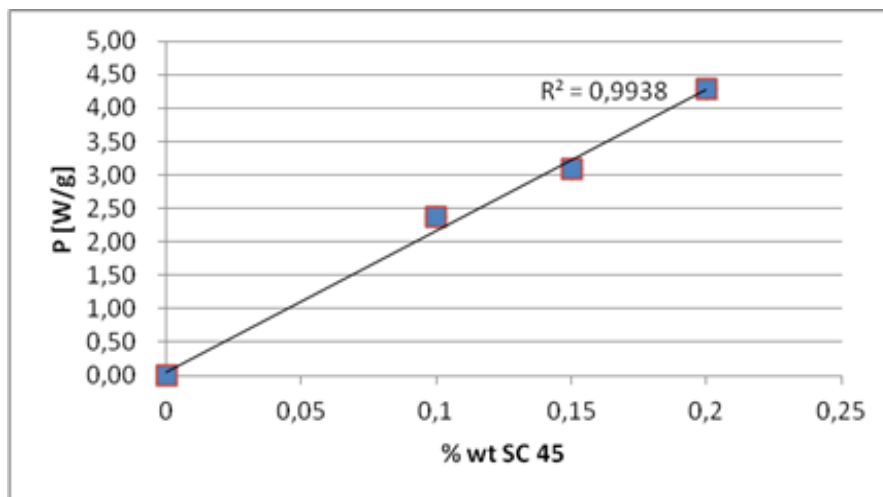


Figure6.14 : Power losses measurements with $B = \text{mT}$ at 220 kHz

Figure 6.14 reports the linear correlation between the increase of SC45 with the specific power losses, with an high value of R^2 .

The preliminary specific power losses evaluations allow to identify the order of magnitude of their quantities taking into account that with the increasing time and temperature of heating the thermal dispersions were not negligible. To reduce this effect the use of a thermal insulating material is needed.

6.2.5.2. Thermal insulation model

By solving the heat transfer equation 5.1.3 ,presented in chapter 5,

$$T = \frac{W}{KS} * \left(1 - e^{-\frac{KS}{Mc}t} \right) + T_r$$

it has been possible to elaborate a graphical solution of this expression. The fitting of theoretical model and experimental one is presented in figure 6.15. A very good interpolation can be appreciated. The graph in figure 6.15 reports the temperature increase as a function of time.

For high time values an asymptotic behavior can be observed, where the curve tends to a saturation temperature and so the trend becomes flat and tends to reach a threshold value at which the generated power is equal to the dispersed one. This condition explains that the heat produced by samples heating and transferred to the water is equal to the heat that is transferred to the environment; in this case, the heat is dissipated through the glass tube where the samples are contained.

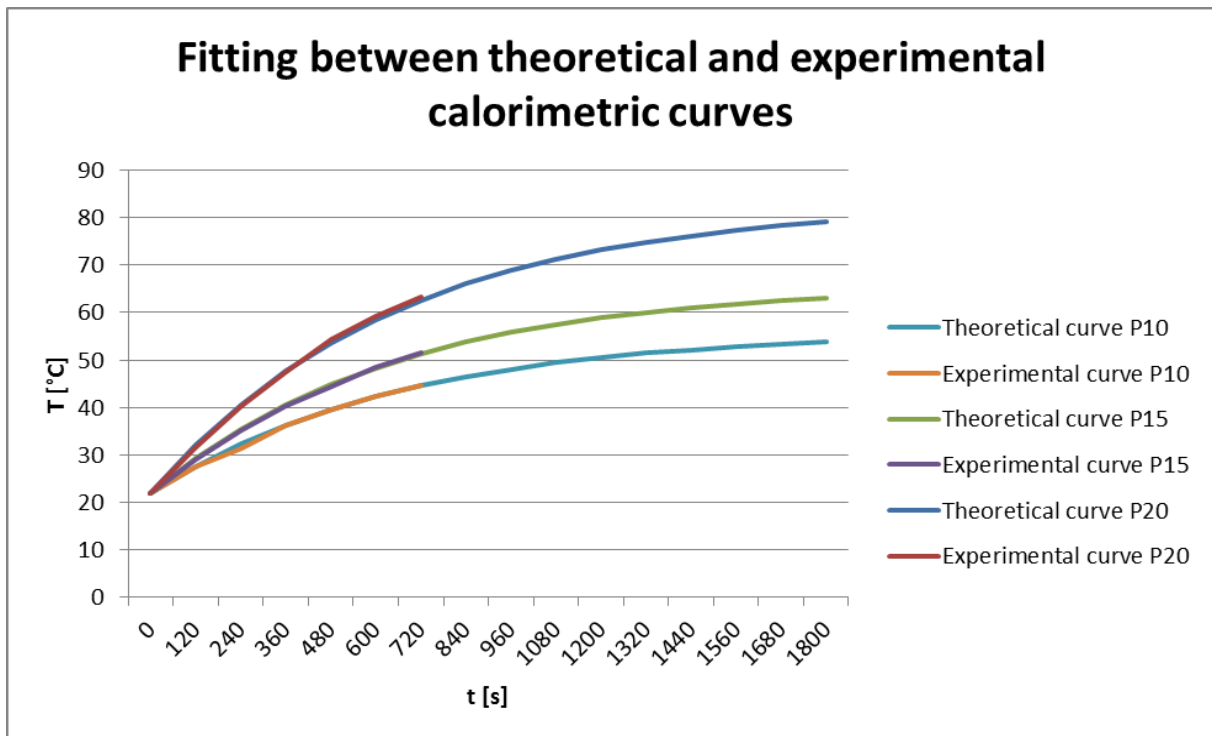


Figure6.15: Fitting of thermal data between theoretical and experimental heating data

This model of dissipation allows the evaluation of saturation temperature for all three proposed cement formulations that must be reached and maintained by modulating all other parameters (working frequency, intensity the magnetic field, exposure time to hyperthermia treatment).

Results and Discussion Composite bone cement characterization

After the aforementioned considerations new calorimetric tests were improved with the use of a thermal insulator around the test tube. It was evaluated the effect of temperature increase at three different values of magnetic fields: at 22,6 mT at 32 mT and at 39 mT (figure 6.16 a-b-c).

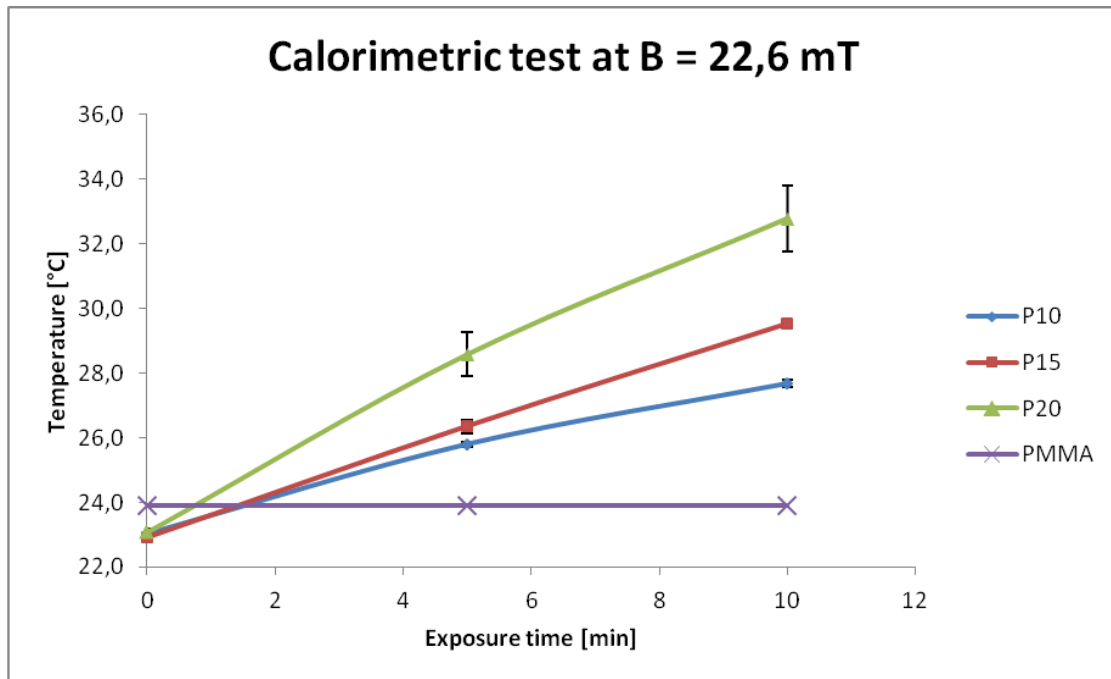


Figure 6.16: Calorimetric tests at 22,6 mT for P10,P15, P20 samples

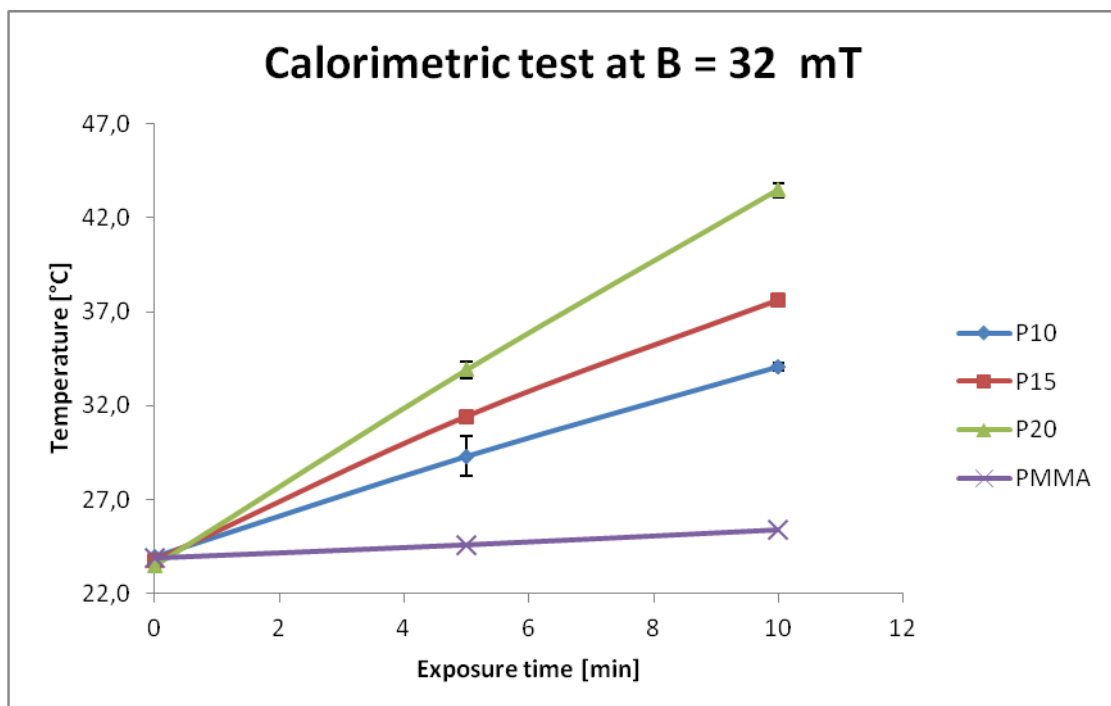


Figure 6.17: Calorimetric tests at 32 mT for P10,P15, P20 samples

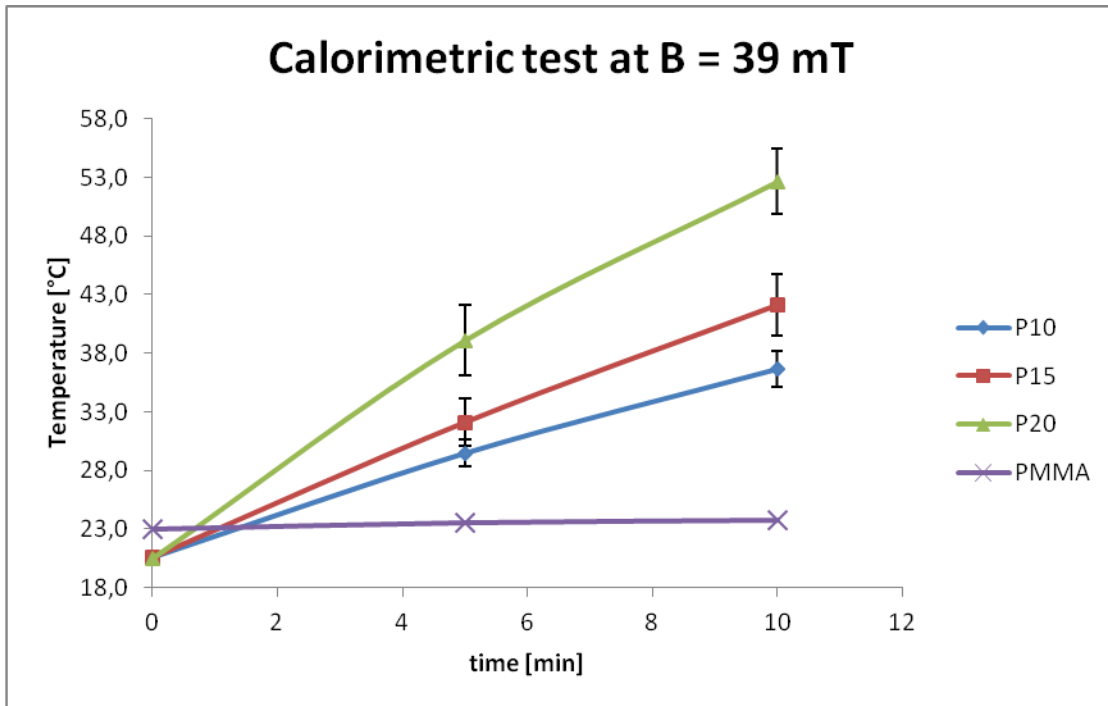


Figure 6.18: Calorimetric tests at 39 mT for P10,P15,P20 samples

The trends of all graphs in figures 6.16, 6.17, 6.18 are changed respect to the preliminary tests. In fact the curves appear as straight lines, in agreement with the intention of dispersion quantification. With the use of the thermal insulator the dispersions are better quantified and the increased water temperatures are higher than in the previous case.

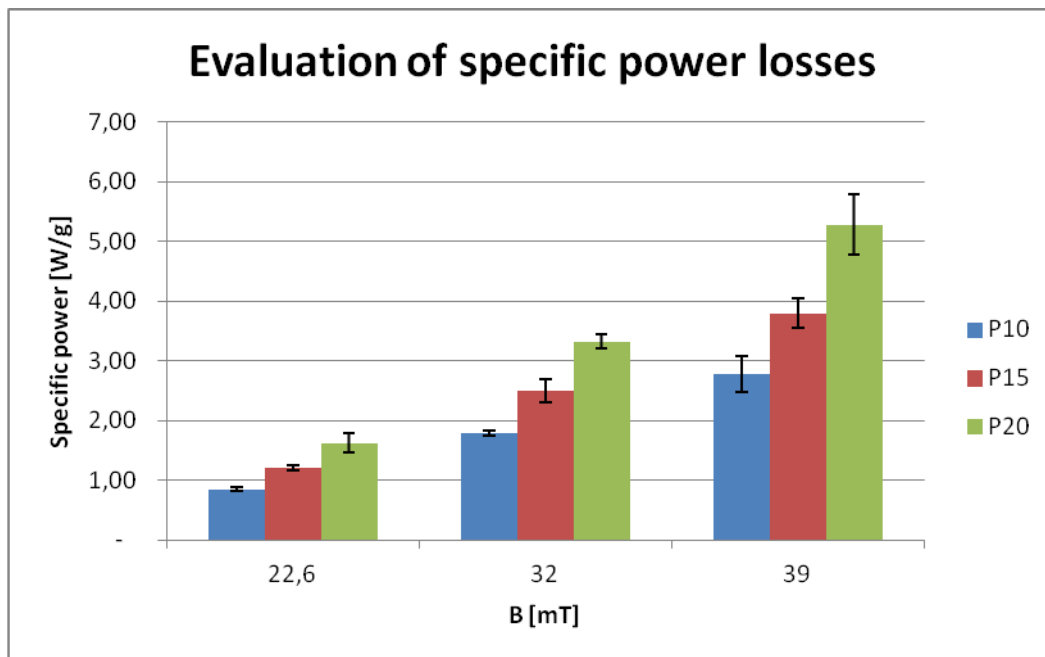


Figure 6.19: Evaluation of specific power losses at 22,6 mT , 32 mT and 39 mT. Measure performed with Egma 6

Results and Discussion Composite bone cement characterization

Figure 6.19 reports the trend of specific power losses at three different values of magnetic field . The measures were evaluated after 600 s of heating. The values are calculated taking into account all the thermal effect generated by the samples, the water, the test tube and the thermal insulator. The values of specific powers increase with the magnetic field for all three formulation and the trend is linear.

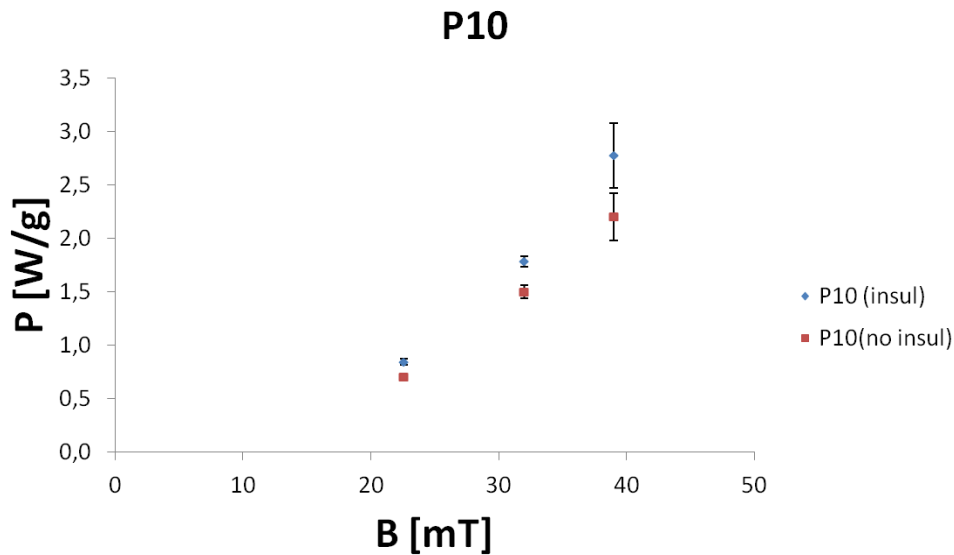


Figure 6.20: Comparison between the evaluation of the specific power losses without thermal insulation (no insul) and with thermal insulation (insul) for P10 sample. Measure performed with Egma 6.

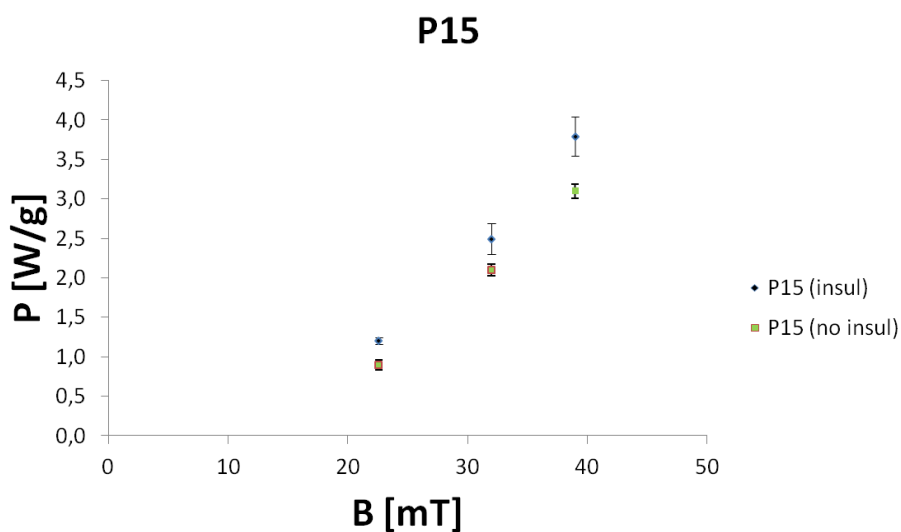


Figure 6.21: Comparison between the evaluation of the specific power losses without thermal insulation (no insul) and with thermal insulation (insul) for P15 sample. Measure performed with Egma 6.

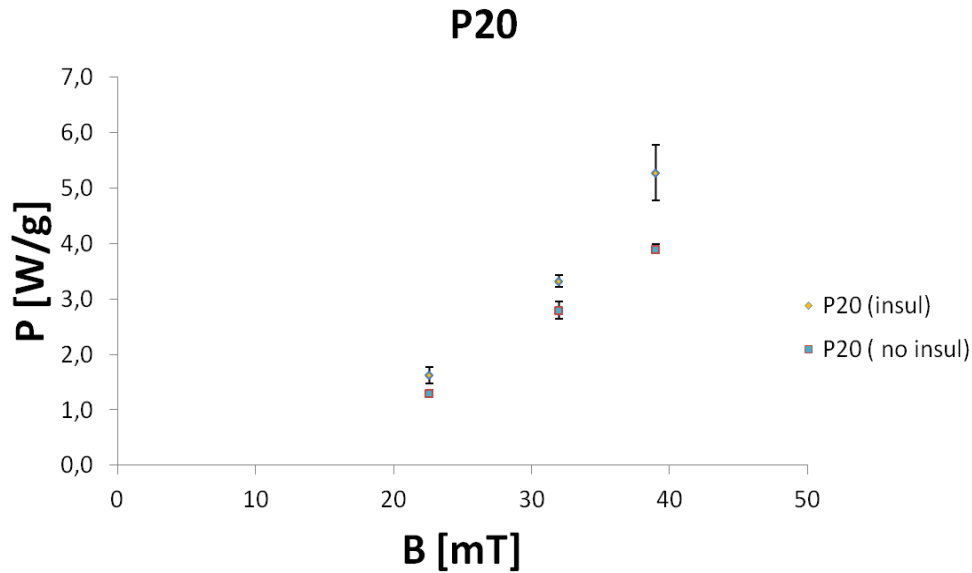


Figure 6.22: Comparison between the evaluation of the specific power losses without thermal insulation (no insul) and with thermal insulation (insul) for P20 sample. Measure performed with Egma 6.

In figures 6.20, 6.21, 6.22 a comparison between the two methods used for the specific power losses evaluation is reported. The presented values have a “scissor trend”, in fact, increasing the magnetic field, the difference between the power losses calculated with thermal insulator and those evaluated without thermal insulator increase. The specific power losses with no thermal insulator are underestimated in respect to the other values, but if we consider the first two power losses values, evaluated with different methods, they remain comparable.

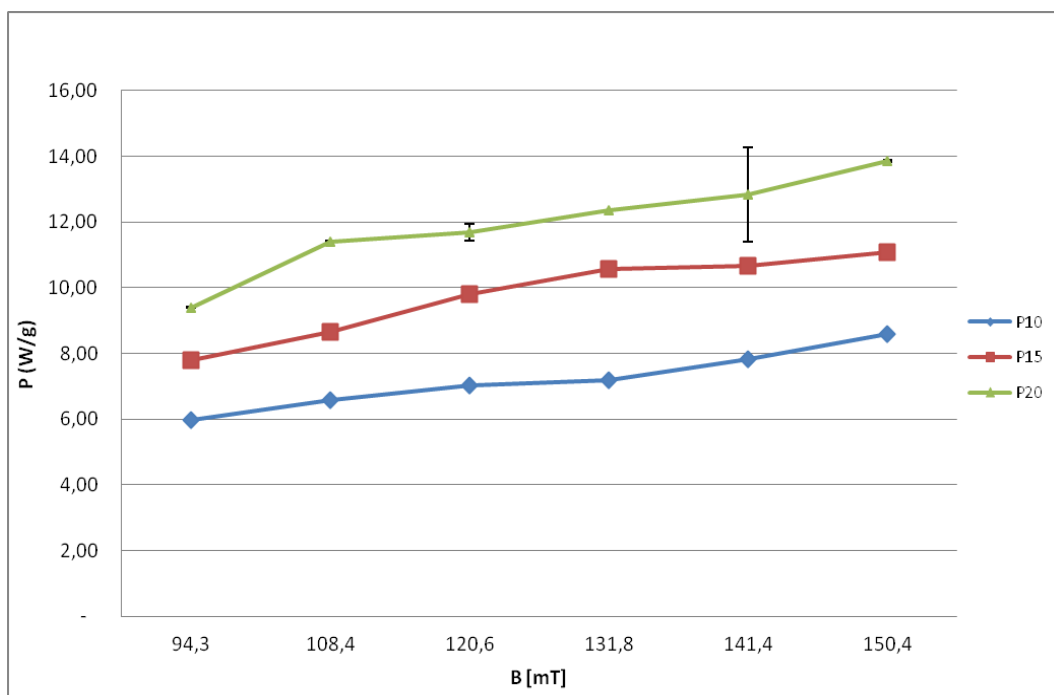


Figure 6.23: Specific power losses evaluation with Egma 30

Results and Discussion Composite bone cement characterization

In order to find an intensity magnetic field range where the variations of specific power losses are smaller, these measurements were repeated with the thermal insulator set up using a more powerful power induction generator (named Egma 30). The machine generates an higher magnetic field up to 150 mT. In figure 6.23 the curve tends to become flat with the increase of the magnetic field. For high values of magnetic field, specific power losses tend to keep constant. When the saturation magnetization is reached the area of the hysteresis loop does not change anymore and thus also the generation of power became constant with increasing field. Probably for high magnetic fields weak eddy current effects also appear, that are seen in the slight slope of the curves in the last part of the graph.

It has been found three different behavior of the specific power loss generated with three applied magnetic fields:

- Low magnetic field 0-90 mT with an exponential growth not with a saturation phenomena
- Intermediate magnetic field 90-130 mT flat profile with a saturation phenomena
- High magnetic field > 130 mT new increase with the appear of eddy current losses.

For *in vivo* future applications it will be preferable to use magnetic field values in a range where the specific power is constant and it is therefore more reliable.

6.2.6. Comparison between calorimetric and hysteresis energy

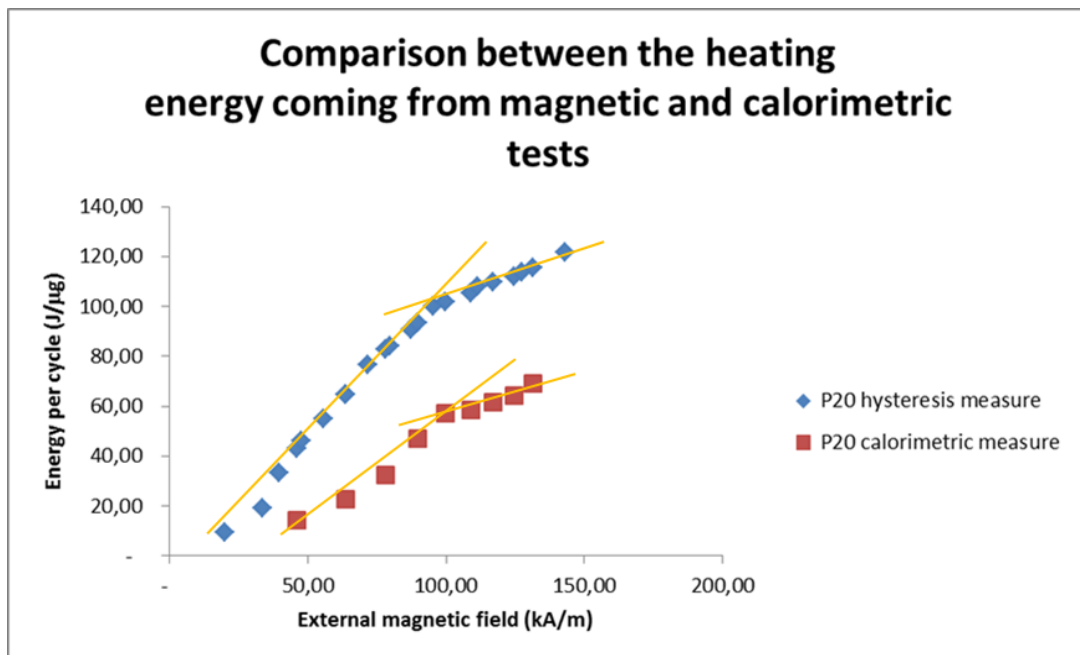


Figure 6.24: Comparison between heating energy coming from magnetic and calorimetric tests

Results and Discussion Composite bone cement characterization

In figure 6.24 a comparison between the energy loss per mass per hysteresis cycle and the energy exchanged in the calorimetric tests was evaluated at different magnetic fields for P20 sample.

The energy exchanged in the calorimetric test is lower than the energy loss in the hysteresis cycle. The working frequency of the calorimetric measurement is 220 kHz, while the hysteresis cycles were measured in DC conditions. The effect of frequency does not allow to reach the DC hysteresis loop. However it permits to achieve an increasing temperature in agreement with Hyperthermia treatment.

From the experimental comparison of the measurements, it has been found that a constant ratio of 0,55 was maintained between the hysteresis and calorimetric curves. With the in frequency test about 50% of the available generated power is lost.

A future improvement will be the optimization of this value with the use of frequency dependent power generator.

6.2.7. Dielectric permittivity measurements

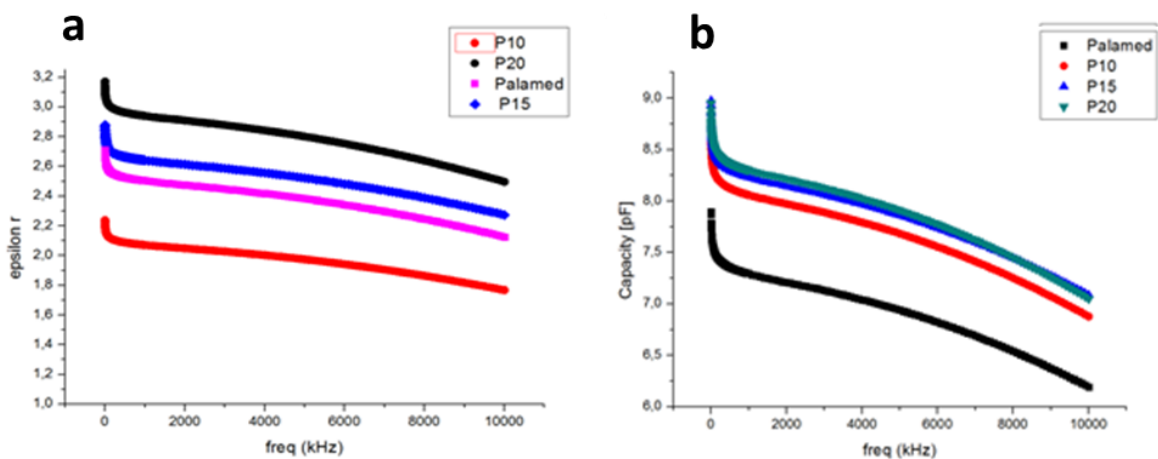


Figure 6.25: Trend of dielectric permittivity ϵ_r and capacity [pF] in the range of 1 – 10 MHz

Figures 6.25a and 6.25b show respectively the trend of the dielectric permittivity and the trend of capacity in pFarad respect to the frequency up to 10 MHz for Palamed® (control material), P10, P15 and P20 composites.

In both graphs, no discontinuity it is seen and all curves show a decrease monotony trend. It can assume that, in this range of frequency (1-10 MHz), all the materials tested do not absorb a specific amount of energy correlated with a specific resonance frequency. The accumulation of energy in the capacitor occurs independently from the investigated frequency. This measure is

Results and Discussion Composite bone cement characterization

aimed to verify that the only magnetic phase that can generate a resonate phenomenon is magnetite. As discussed in [9-10] the resonance of magnetite is among between 1-10 GHz. But, since the resonant frequency also depends greatly on the size of the particles and the chemical composition of the magnetic phase, this measurement was necessary to verify the absence of any resonant phenomenon in these range of frequencies. Moreover, these impedance measurements permit to affirm that the heat generation depends only from hysteretic phenomena. Wider is the hysteresis cycle and wider will be the heat generation independently from the frequency stimulation between 1-10 MHz.

6.2.8. Magnetic permittivity measurements

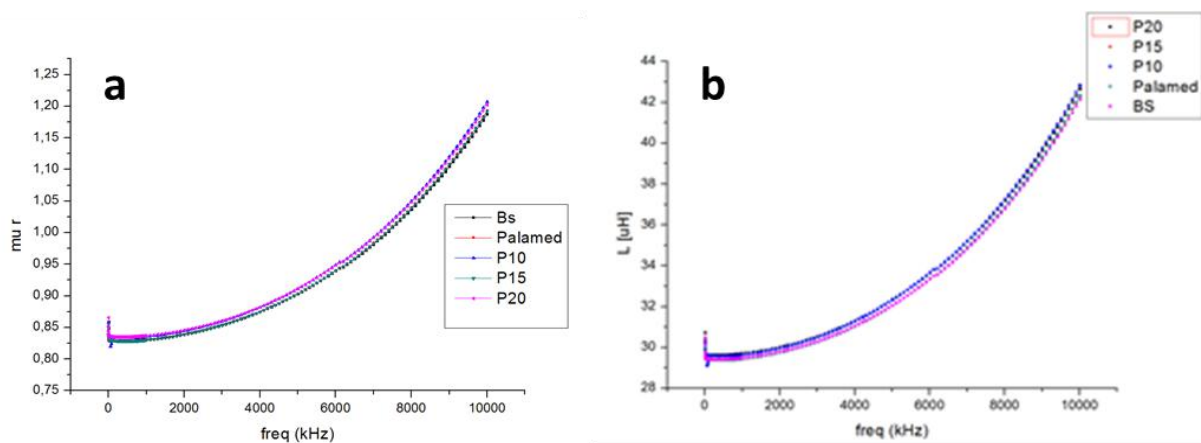


Figure 6.26: Trend of magnetic permittivity (μ_r) and inductance L [μH] in the range of 1-10 MHz

The magnetic permeability indicates the ability of a material to conduct magnetic flux. The continuity of the inductance L respect to the frequency confirmed the same results of capacity in the same range of frequency. The curves don't present any discontinuity connected with resonance frequency. (figure 6.26)

In conclusion the electric and magnetic response of the composite material is independent from the frequency in the range of 1 – 10 MHz. In this scenario it's clear that there is not a specific radiofrequency for an efficient heating. So in calorimetric measurements any frequency in this range could be used.

6.2.9. Hyperthermia treatment simulation

The results in figure 6.27 evidence the reaching of an equilibrium condition, in which the heat generated from the sample is equal to the heat dispersed by the environment gaining and

Results and Discussion Composite bone cement characterization

maintaining a constant temperature around $42^{\circ}\text{C} \pm 1$. At thermal equilibrium the temperature keeps itself constant (in a range $\pm 1^{\circ}\text{C}$) and it is independent from the exposure time to a magnetic field of 22,5 mT, so it may be defined according to a therapy protocol.

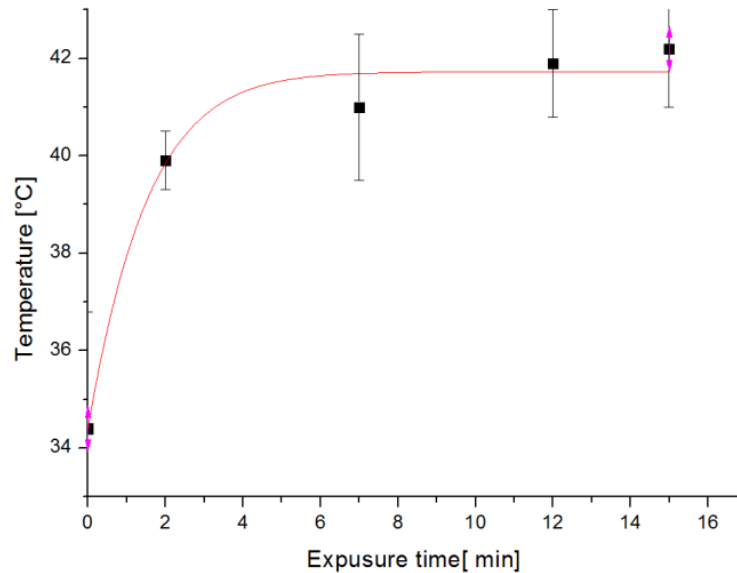


Figure 6.27: Experimental curve which shown a stabilization of the temperature at 42°C about for 20 minutes

6.2.10. Heat transfer simulation with Comsol Multiphysics®

In figure 6.28a a color model of the heat distribution is shown. Results simulate the temperature that the cells will be subjected to, under magnetic induction hyperthermia. The maximum temperature value is seen on the upper surface of the sample. In figure 28b-c the graphics of the mean temperature of the lateral and upper surface of the P10 sample are reported. These surfaces are supposed to be those on which the tumoral cells will be seeded. They presents temperatures able to induce a damage to metastatic cells due to hyperthermia treatment [18]. The temperatures trend in figure 6.28b-c is the same of that measured with Infrared camera (figure 6.27).

Results and Discussion Composite bone cement characterization

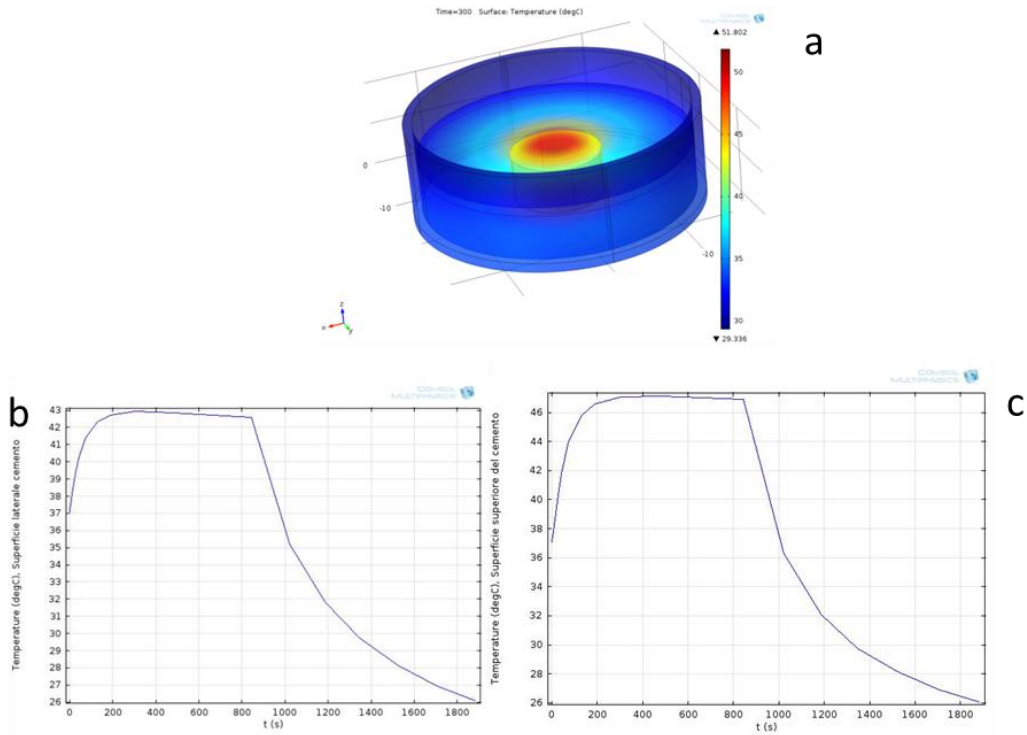


Figure 6.28: Results of finite element model of P10 sample: field of temperatures after 300 s of heating (a), mean temperature of the upper surface sample (b), mean temperatures surface of the lateral sample (c)

In figure 6.29 a-b the thermal dose CEM43 vs time plots is evaluated and results are in agreement with Yuan article [19]. The highest value of CEM is reaches for the upper surface of sample.

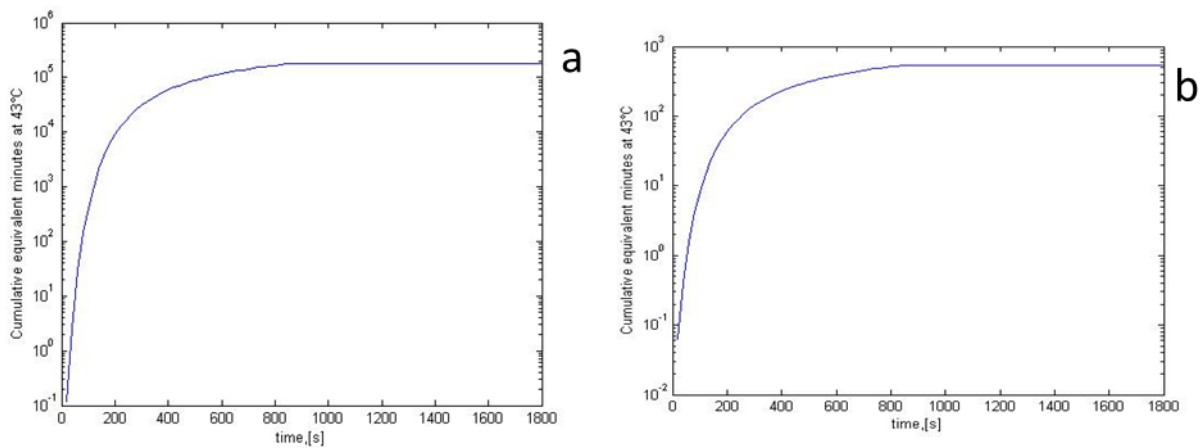


Figure 6.29: CEM at the upper surface (a), CEM at the lateral surface (b)

6.2.11. Mechanical Tests

6.2.11.1. Uniaxial compression test

The test evidences a slight decrease of compression strength for the composite cements respect the commercial samples (see in figure 6.30); however the obtained values are clearly higher than the limit value of 70 MPa required from the standard ISO 5833-2002 .

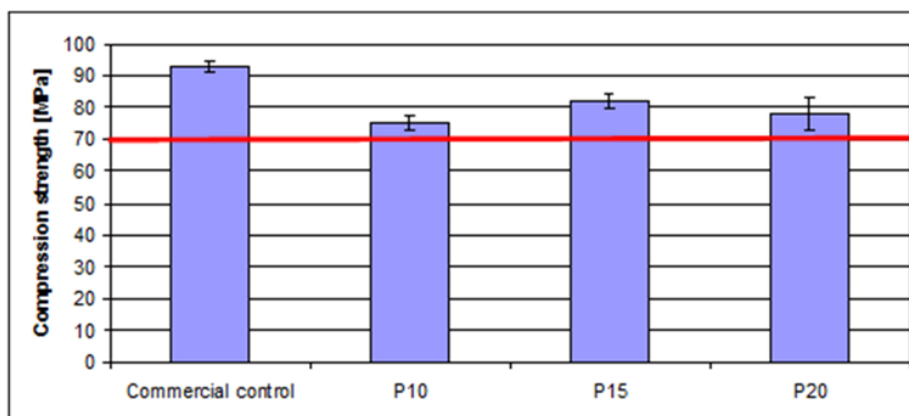


Figure 6.30: Compression strength evaluation for bioactive and ferrimagnetic composite bone cements (P10, P15, P20) and commercial control samples.

The presence of a glass-ceramic phase decreases the compressive strength respect to the control for all three formulation but without creating any statistical difference between the samples. The small particles size of a glass ceramic, which can create structural discontinuity, and the presence of porosity, influence the results.

6.2.11.2. Four point bending test

The bending strength (B) and modulus (E) are reported in figure 6.31; as can be observed the bending strength of the composite cements is lower than those of the commercial cement. The introduction of SC45 seems to slightly decrease the flexural strength of the material, although the values obtained for the P10 and P15 samples satisfy the ISO requirements ($B > 50$ MPa) as well as the bending modulus of the all composite cements ($E > 1800$ MPa).

Results and Discussion Composite bone cement characterization

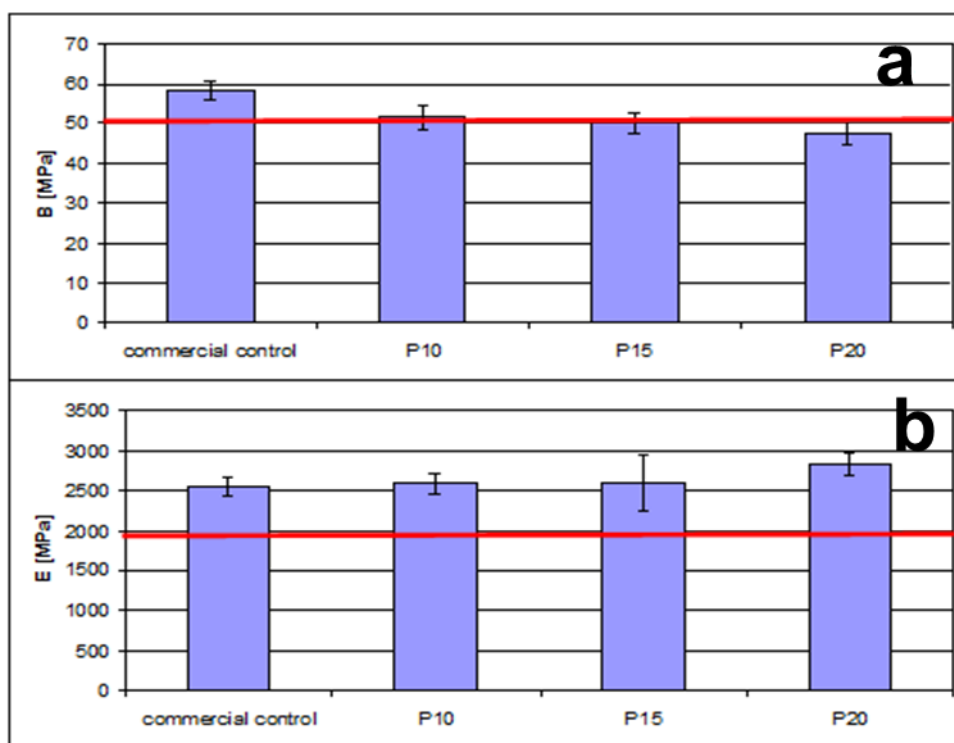


Figure 6.31: Bending strength (a) and modulus (b) evaluation for bioactive and ferrimagnetic composite bone cements (P10, P15, P20) and commercial control samples.

However P20 sample obtains higher bending modulus respect to the other composite. The diagram in figure 6.31a shows the decrease of bending strength versus the increase of SC45 in the polymer matrix in fact adding of high percentage of ceramic phase give the composite brittle. It can be stated that the composition of P20 is a threshold sample as the value of flexural strength and so it must be used a lower %wt of SC45 for relevant structural application.

6.2.12. Characterization of fracture surface after bending test

The fracture surfaces of the samples with minimum, maximum and medium value of flexural bending stress are analyzed by means of SEM-EDS analyses. Figure 6.32 reports the medium one as an example. Any significative difference was noticed on the other fracture surface images respect to the following results. Figure 6.32a–c shows the control samples in which the micro porosity and the radio-opaque agent with a very fine particles (figure 6.32b,c) are evident. These samples obtain the highest bending strength when compared to the composites. Figures 6.32d–f represent P10 sample, figures 6.32g–i P15 and figures 6.32j–l P20 at different levels of magnification. The glass ceramic phase, present in all samples from 10%wt to 20%wt, is well dispersed in the PMMA matrix; nevertheless a decrease in the bending strength is observed for

Results and Discussion Composite bone cement characterization

the composites cement respect the control sample. It is possible that the particles of SC45 conferred to the biomaterials a brittle behavior because they represent a discontinuity point that could transform into critical defect during the development of the mechanical test and support the opening and propagation of the crack along the fracture plane, as can be seen in figure 6.32m for sample P20 at 2000x (see the white arrows).

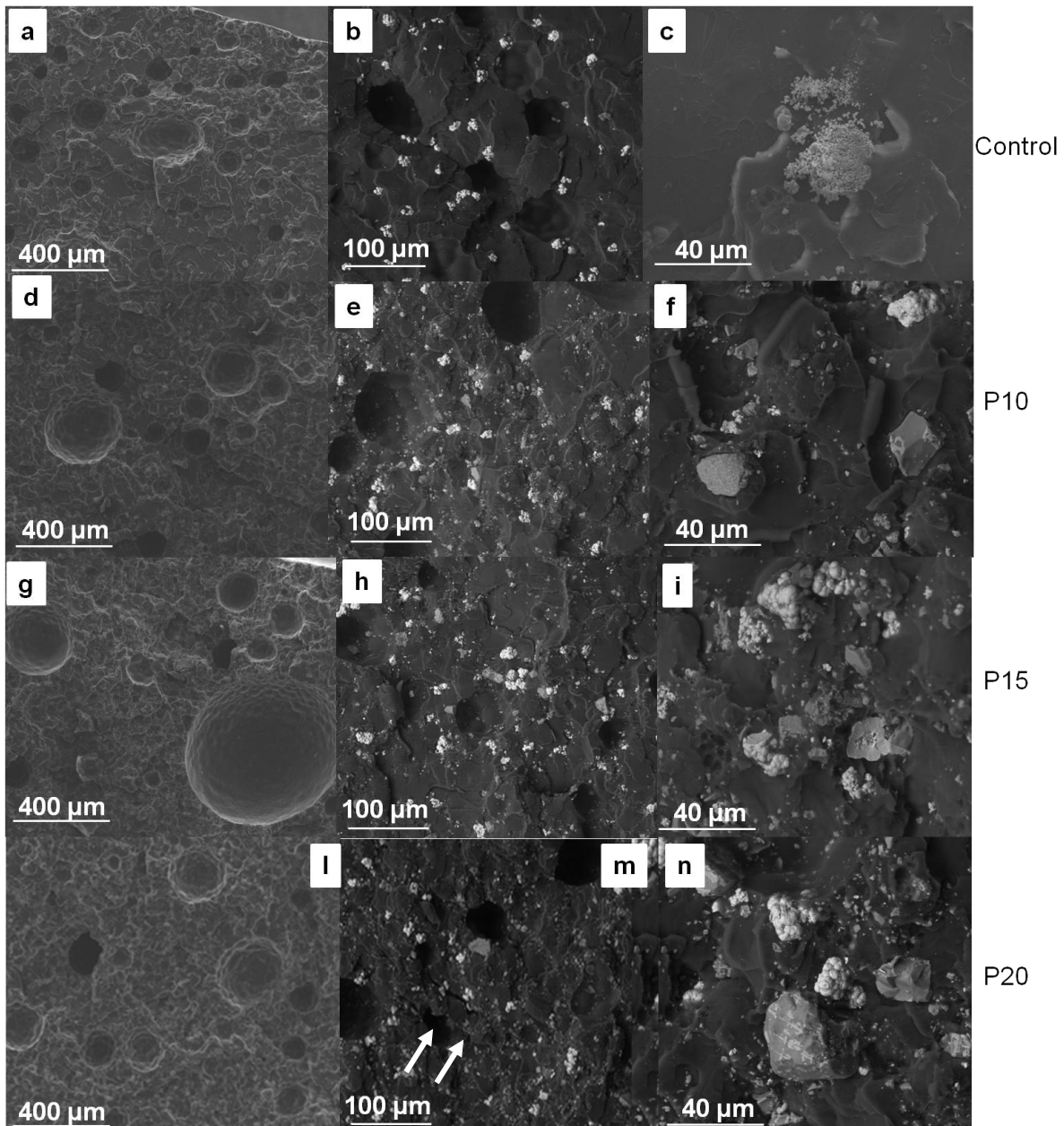


Figure 6.32: SEM surface fracture: (a), (b), (c) control surface at 200x, 500x, 2000x, respectively; (d), (e), (f) P10 surface at 200x, 500x, 2000x, respectively; (g), (h), (i) P15 surface at 200x, 500x, 2000x; (j), (k), (l) P20 surface at 200x, 500x, 2000x.

Any eventual aggregation phenomena will be a weak point for the bending fracture and therefore for not degrade the mechanical properties it is required the synthesis of well mixed composites with low wt% of SC45.

6.2.13. Biological characterization

SC45 was already tested for its bioactivity and in a previous work for the biocompatibility showing a high degree of citocompatibility [3].

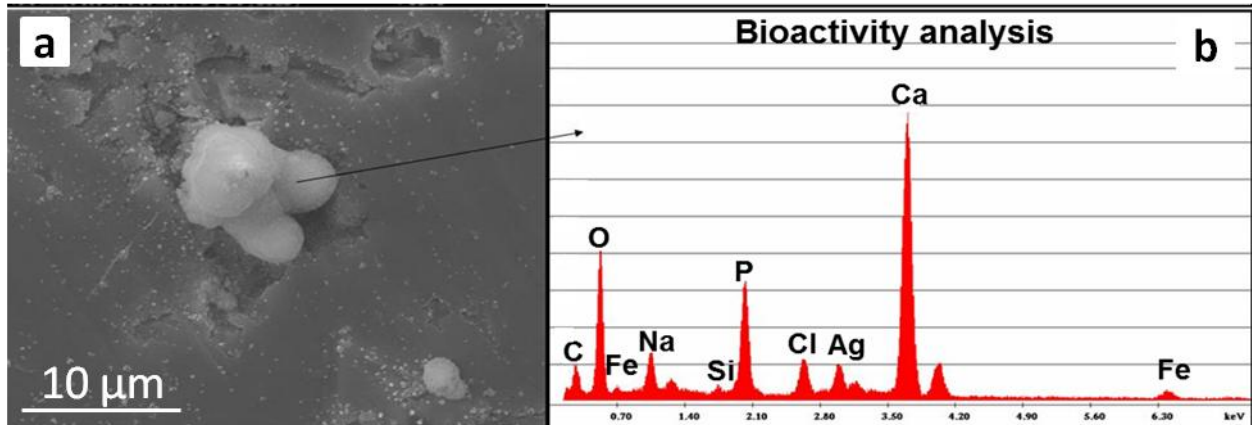


Figure 6.33: On the left morphological and on the right compositional analysis of SC45 after soaking in SBF for one month[3]

In figure 6.33 the SEM image evidences, after one month of soaking in simulated body fluid (SBF), a precipitate of a phase rich in calcium and phosphorous similar to apatite observed on a bulk of glass ceramic surface and the compositional analysis shows an increase in calcium and phosphorus. As reported in literature [2], this behaviour is commonly related to the ability of stimulating bone regeneration *in vivo* due to the glass composition, which is based on 45S5 Hench formulation.

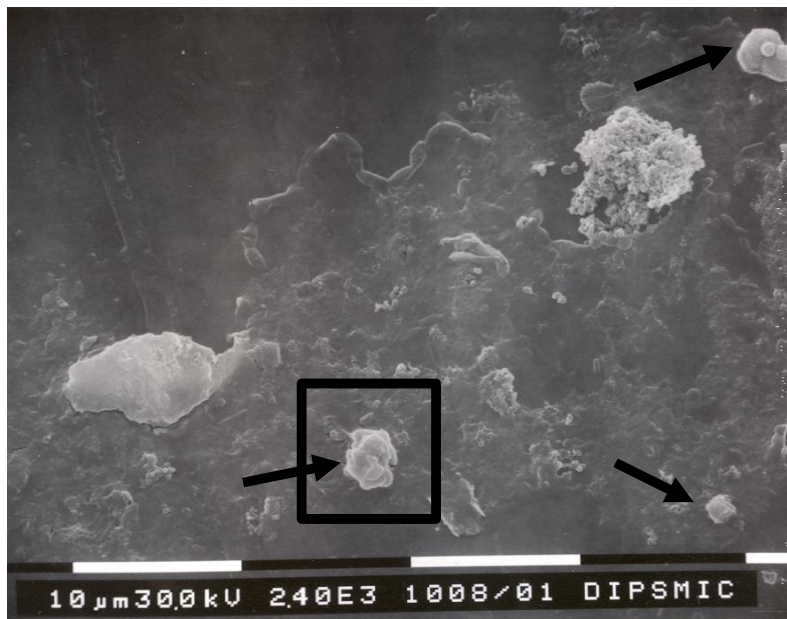


Figure 6.34: SEM micrograph of a bulk surface samples of glass-ceramic SC45 after soaking in SBF for 1 month[12]

Results and Discussion Composite bone cement characterization

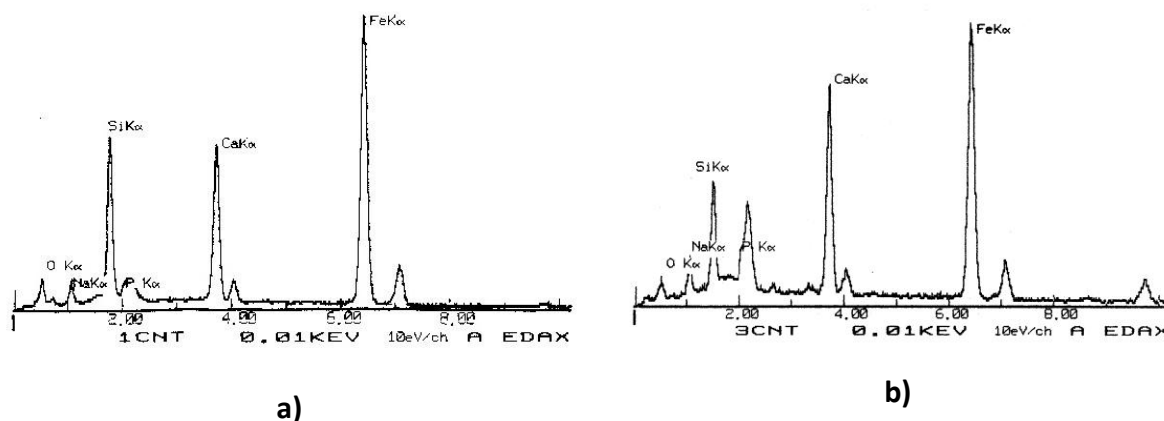


Figure 6.35: Local EDS analysis of surface of SC45 sample a) before and b) after soaking in SBF for one month.[12]

Another example of SC45 bioactivity after soaking in SBF for one month is presented in figure 6.34. A non-homogeneous layer of a P and Ca rich precipitate could be seen (see arrows). The presence of this precipitate was tested by EDS analysis. Local analysis of this sample before soaking in SBF is illustrated in figure 6.35a. The EDS analysis of the marked area of the sample (see figure 6.35) after one month of immersion in SBF is presented in figure 6.35b.

Before immersion in SBF, the predominant peaks were those corresponding to iron, silicon and calcium. The intensity of phosphorus peak was very low.

It could be noted that after soaking in SBF, phosphorus and calcium intensities increased, due to the formation of the precipitates. The other ions (iron, silicon and sodium) were still present.

Therefore, for SC45 a non-uniform Ca and P rich layer is formed after 4 weeks. The kinetics of the surface reactions is slow, probably due to the higher concentration of iron ions in the matrix. Iron ions could play different roles in the bioactivity process:

- They can inhibit the ion exchange process of sodium and calcium avoiding the coming out of them from glass network.
- A generation of iron solid solutions can occur.
- The presence of iron could decrease the solubility of the glass so that no silica-gel rich layer formed.
- The absorption of this into the calcium and phosphorus sites inhibited the nucleation and growth of hydroxyapatite.

6.2.13.1. Osteointegration test: *in vitro* bioactivity

In order to demonstrate the osteointegration capability of the composite cements, an *in vitro* bioactivity test is performed, with the same approach already used for the pure glass-ceramic [2]. The samples are soaked in simulated body fluid (SBF) which represents the inorganic component of the blood plasma, as described in the “materials and methods” section. The bioactivity process depends on:

- The presence of the SC45 particles, because PMMA does not generate any osteointegration reaction,
- on how much the glass particles are exposed at the cement surface,
- the ability in the promotion of the ion exchange mechanism that is essential for the development of a mineralized surface.

Each composite cement, after immersion for 4 weeks in SBF, is gently washed, dried at room temperature and subjected to surface morphology investigation (SEM) and compositional analyses (EDS).

On each kind of composite, two types of precipitates can be observed, both typical of the various steps of bioactivity [11].

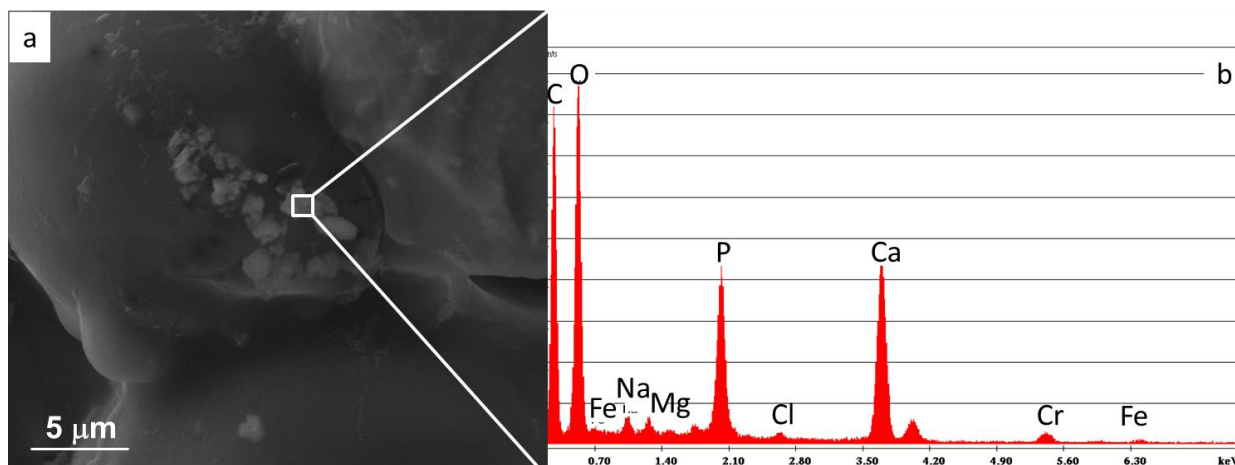


Figure 6.36: morphological (a) and compositional (b) analysis of P10 sample after SBF treatment

Figure 6.36 reports a morphological and compositional analysis of some precipitates seen on the P10 surface. The EDS in figure 6.36b shows an enrichment of calcium and phosphorus, which is an indication of bioactivity process. These precipitates could be identified as precursor of hydroxyapatite. The high peak of carbon comes from the polymer.

Results and Discussion Composite bone cement characterization

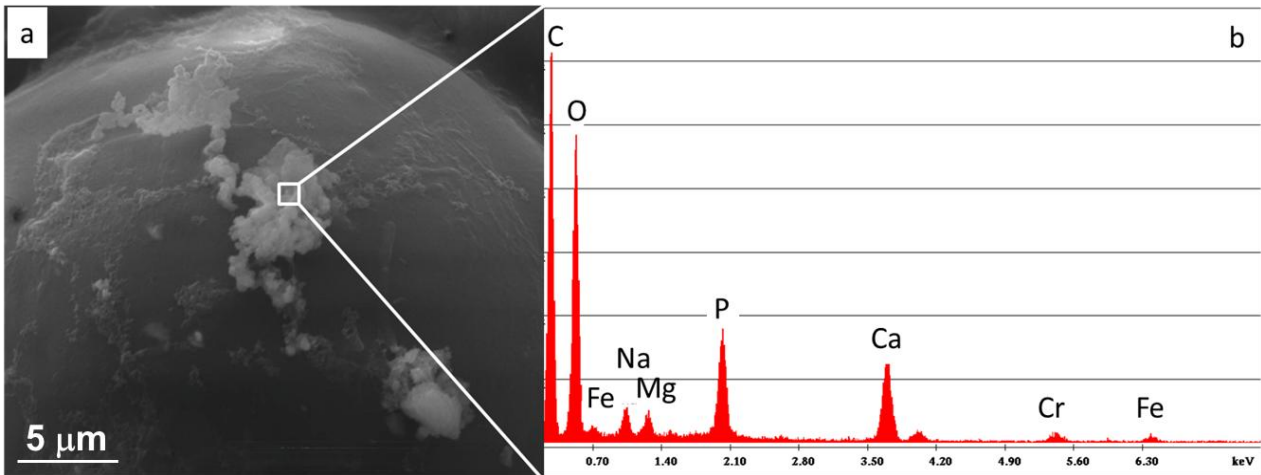


Figure 6.37: morphological (a) and compositional (b) analysis of P10 sample after SBF treatment

Another similar behavior could be observed in figure 6.37, where a morphological and compositional analysis is performed on some precipitates. Also in this case the peaks of calcium and phosphorus in the EDS spectrum are very high, this analysis evidences the precipitation of phases rich in Ca and P, precursors of hydroxyapatite (HA). The morphological analysis of the precipitates in figure 6.37a matches quite well with the fourth step of bioactivity process where a preliminary amorphous layer rich in Ca^{2+} , PO_3^{-2} and CO_3^{-} ions appear on the material surface.

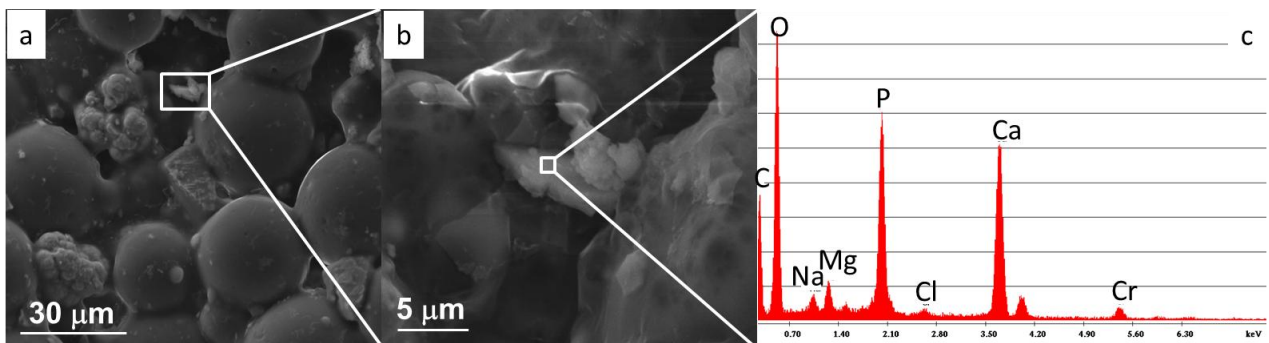


Figure 6.38: morphological (a-b) and compositional (c) analysis of P10 sample after SBF treatment

Figure 6.38 evidences the presence of zone containing precipitates rich in calcium and phosphorus (as evidenced with EDS analysis) on a sample surface. Probably under this precipitate there is an

Results and Discussion Composite bone cement characterization

exposed glass ceramic particle, which induce its formation.

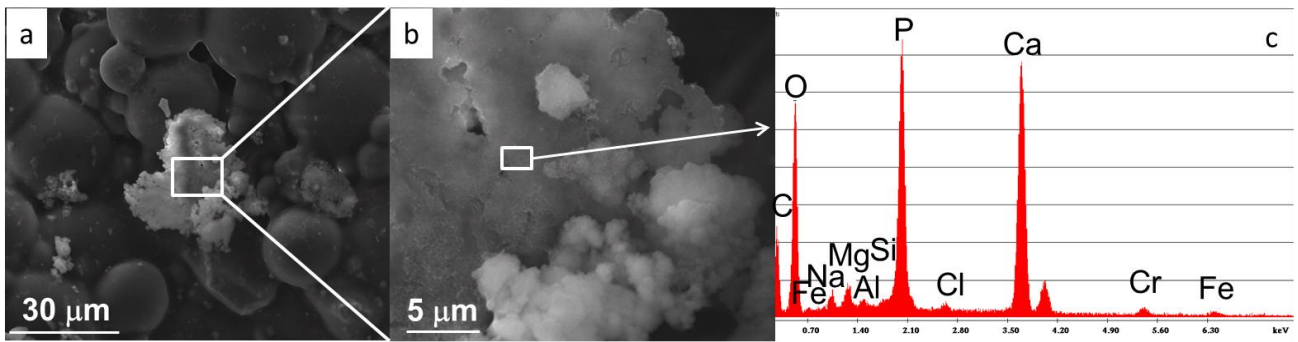


Figure 6.39: morphological (a-b) and compositional (c) analysis of P10 sample after SBF treatment

Figure 6.39 presents another different morphology of precipitates observed on composite P10: it is possible to see a compact layer containing calcium and phosphorous, which cover a wide area of sample. The structure of the precipitates tends to a globular shape, similar to the HA one.

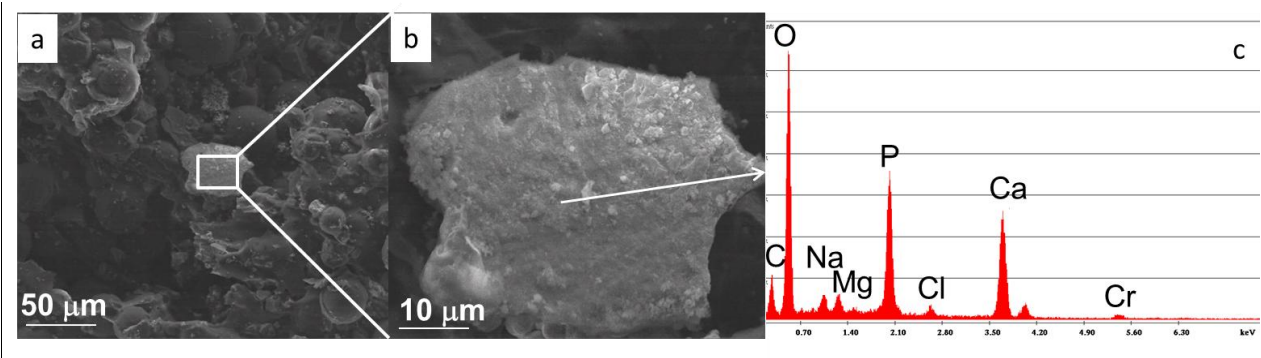


Figure 6.40: morphological (a-b) and compositional (c) analysis of P15 sample after SBF treatment

Figure 6.40a evidences a wide layer of calcium and phosphorus precipitates on P15 sample. In the magnification in figure 6.40b the presence of spherical particles is seen. EDS analysis confirms the presence of Ca and P on this precipitate.

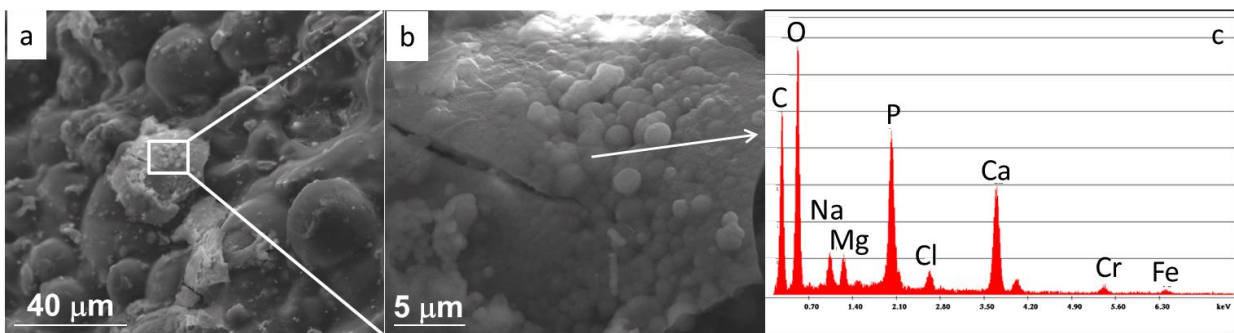


Figure 6.41: morphological (a-b) and compositional (c) analysis of P15 sample after SBF treatment

Figure 6.41 shows the presence of some agglomerates, with the typical globular morphology of microcrystalline hydroxyapatite. In fact, the EDS analyses performed on this kind of precipitates,

Results and Discussion Composite bone cement characterization

reveals the presence of very intense peaks of P and Ca. The magnesium peak is due to the incorporation of this element on HA structure[3], while Na and Cl are due to the presence of NaCl formed during the immersion in SBF.

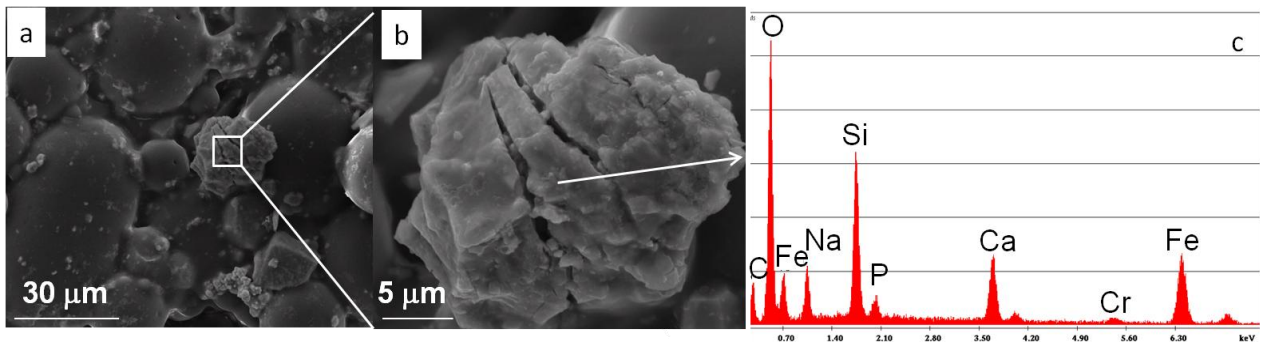


Figure 6.42: morphological (a-b) and compositional (c) analysis of P20 sample after SBF treatment

The SEM-EDS analysis performed on P20 sample (figure 6.42a) demonstrates the presence of a particle rich in Si and Ca. This particles present all the elements characteristic of the glass ceramic; however Si, Ca and O peaks are prevalent, this could indicate a possible silica gel layer enriched in calcium present on a SC45 particle.

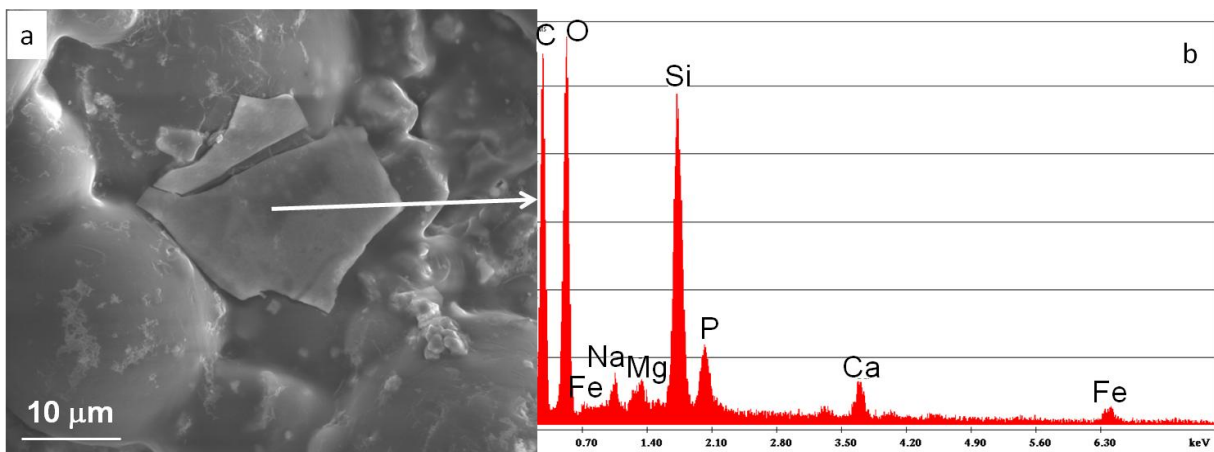


Figure 6.43: morphological(a-b) and compositional (c) analysis of P20 sample after SBF treatment

Figure 6.43a documents the presence of a thin silica layer on the P20 surface. The morphology of the layer is supported by the EDS analysis in figure 6.43b where high peaks of Si and O are observed.

As previously reported, the presence of magnesium in the precipitates, observed in all composite cements, is due to its inclusion on HA or its precursors during the bioactivity process..

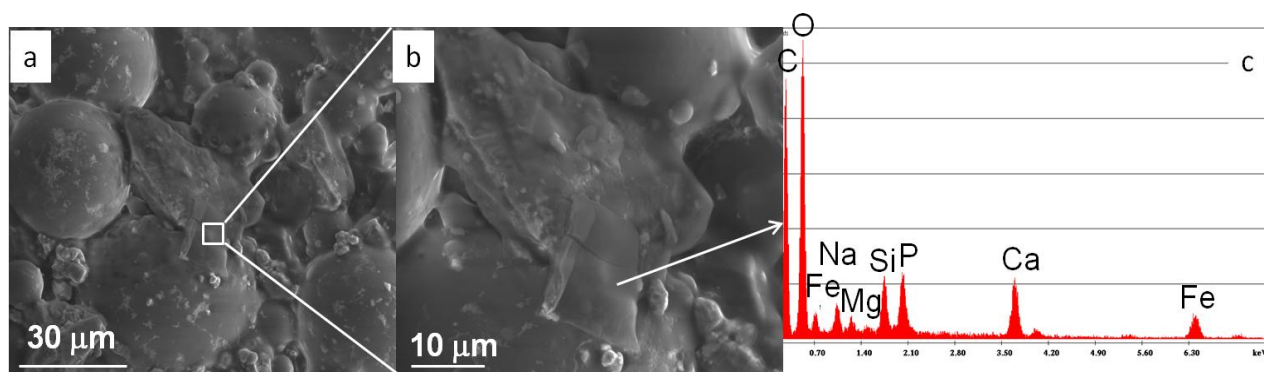


Figure 6.44: SEM micrographs (a, b,) and EDS spectra (c,) of the precipitates observed on the P20 composite cement surface after 4 weeks of soaking in SBF.

In figure 6.44a a typical flat morphology of silica-gel is seen; is the silica-gel layer forms during the first steps of bioactivity: after a rapid ion exchange between the glass ceramic particles exposed on the cement surface and the solution, silanols are generated on the glass surface and, by polycondensation, a silica gel layer develops [12]. This layer is a first substrate that promotes the adsorption of Ca^{2+} and PO_4^{3-} ions from the solution. The EDS pattern of figure 6.44c reveals high peaks of Si, Ca and P, evidencing the enrichment on Ca and P of SiO_2 layer .

As reports in [3, 13] the SC45 glass-ceramic bioactivity is slow; moreover the glass particles are dispersed in the Palamed® matrix so only a part of them are completely exposed on the cement surface. For these reasons it is not surprising that different kinds of precipitates are still observed after 4 weeks because the composite is not completely covered by mature HAp.

In order to investigate the presence of calcium and phosphorus on the cement surface, a structural investigation (by XRD) of the surface of the samples after the SBF treatment is performed. Due to non-completely-planarity, high roughness of the cement, the presence of zirconia and the non-uniformity of CaP precipitate on the surface, it is not possible to distinguish and identify one or more calcium phosphate phases .

These results are, in any case, sufficient to asses that the addition of SC45 confer bioactive properties to the composite bone cements.

6.2.14. Leaching test

The amount and kinetics of iron release are investigated by dipping P20 and control samples in SBF and analyzing an aliquot of spilled solution at 3 hours, 1, 3, 7, 14 and 33 days with GF-AAS. The obtained results demonstrate a Fe release in the range of 0,6-1 $\mu\text{g/l}$ for all samples and time periods, this value is comparable with the LOD (Limit of Detection) of the used instrument and is

ascribable to the Fe contained in the saline buffer used for the experiment. This is a reassuring result, since let us asses that any iron overloading should not be expected by the *in vivo* application of the composite bone cements.

This result has two main implications. The first one is that the iron, which is not transformed in magnetite is not leached into the saline solution but it remains embedded into the amorphous matrix, without creating possible toxicity problems for cells. The second one concerns the possibility of iron ion to enter into the glass network and take the place of silica. Iron could become a former ion in the formation of glass network. The hypotheses are in agreement with leaching and viability tests and with evaluation of %wt of magnetite into the glass by XRD and saturation magnetization. From the last two characterizations the same amount of magnetite was evaluated equal to about 28% wt. which was far from a stoichiometric amount. For these reason a recombination of iron can be possible.

6.2.15. Cytocompatibility evaluation

These tests are performed under the coordination of Prof.ssa Lia Rimondini and Dr. Andrea Cochis in the Department of Health Science at the University of Eastern Piedmont "A.Avogadro" (No).

The SC45 was preliminarily characterized in terms of citocompatibility in a previous work [3], on 3T3 murine fibroblasts cell line. In the mentioned research work it was observed a biocompatible behavior of the glass-ceramic, even if lower than that of polystyrene control, and a pre-treatment in aqueous solutions was necessary in order to assure no sign of cytotoxicity.

An *in vitro* biological characterization is performed on the composites to analyze the behavior of the bone cement loaded with this glass-ceramic. All the tested samples (P10-P15-P20) enriched with the bioactive glass-ceramic result as highly cytocompatible with human osteoblasts (Mg63). In the indirect assay, no significant differences are noticed between control (Palamed®) and tested samples; cells viability results in a range from 95 to 97% for all the chosen time-points of 24, 48 and 72 hours (figure 6.45 a-c). This finding suggests that from the composite bioactive samples no toxic elements have been released into the medium during the 7 days of pre-treatment in the serum free DMEM.

Results and Discussion Composite bone cement characterization

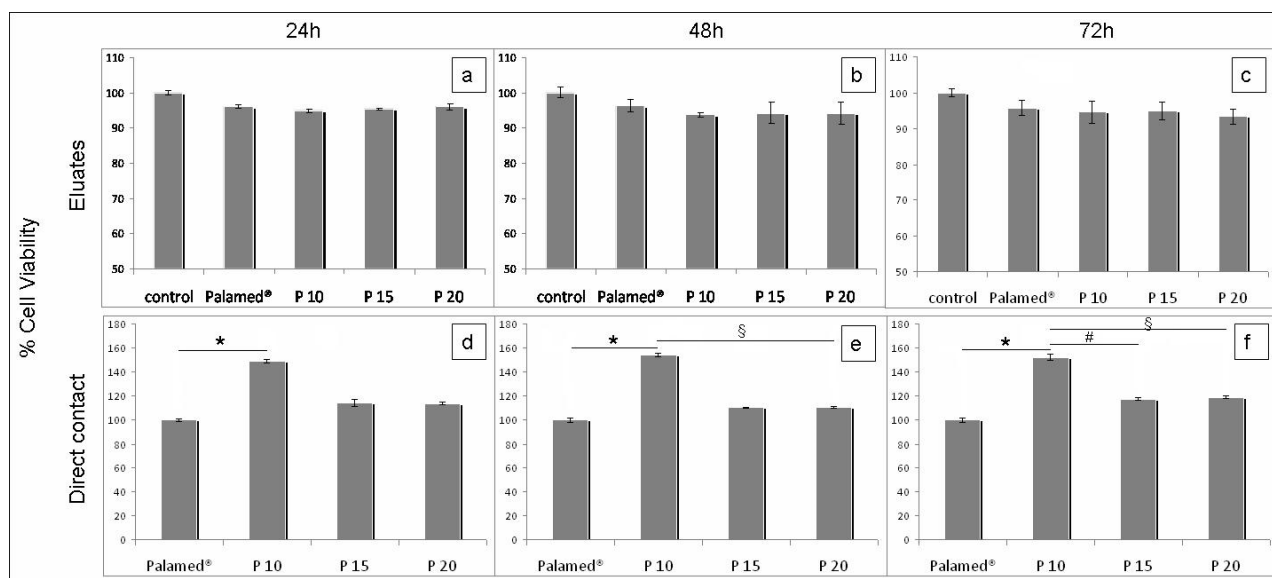


Figure 6.45: Human osteoblasts viability evaluation. Cells viability after 24 (a), 48 (b) and 72 (c) hours of cultivation in the indirect assay; no statistically significant differences were noticed between the groups ($p > 0.05$). On the opposite, in the direct assay a significant difference was noticed between P10 and controls after 24 (d), 48 (e) and 72 (f) hours ($p < 0.005$, indicated by *). Moreover, a significant difference was noticed between P10 and P20 at 48 and 72 hours ($p < 0.05$, indicated by §) and between P10 and P15 after 72 hours ($p < 0.05$, indicated by #). Bars represent means and standard deviations.

The direct cytocompatibility assay shows encouraging results regarding the viability of cells seeded directly onto samples surfaces. In fact, in comparison with controls, no loss of viability is reported; moreover, the viability value of P10 sample results statistically significant compared to controls at each time-points (figure 6.45 d-f, indicated by the * symbol). Interesting statistically significant differences are noticed also between P10 and P20 after 48 and 72 hours (indicated by the § symbol) and between P10 and P15 after 72 hours (indicated by the # symbol).

These data confirm that the addition of the SC45 glass ceramic into the commercial PMMA-based bone cement has not affected its cytocompatibility for all the formulations (P10, P15, P20). Particularly, P10 results as the best one in term of cells viability. This result could be tentatively related to morphology features (such as the surface roughness, which could be different at the microscopic level if different amounts of glass-ceramic powders are exposed) which must be investigated, as well as to a combination of chemical and magnetic effects. Specifically, the formulation P10 containing the lower content of bioactive glass-ceramic and it is potentially prone to a lower release of ions in comparison to P15 and P20. Since, in the early stages of bioactivity, ion leaching could negatively affect the cell behavior [14], and only after the formation of the first bioactive surface layers cells colonize the area. The reason of the better cytocompatibility of P10 in respect to P15 and P20 could be found in its more controlled reactivity.

Results and Discussion Composite bone cement characterization

On the other hand, the best performances of P10 in comparison to the control could be related to the magnetic field generated by magnetite inside the glass-ceramic that is “sensed” by the cells [15, 16], with a positive effect on their viability.

This hypothesis is supported by the fact that the better behaviour of P10 is observable only in the direct contact assay. These considerations let hypothesize that the P10 formulation represents a good compromise among bioactivity, biocompatibility and improvement of cell viability. Future investigations will be necessary for better understand the reason of this preliminary result by scheduling specific biological tests which can discriminate the eventual role of magnetic field on cell viability.

Also cells morphology, adhesion and density result comparable between controls and composite samples, when visual observation by light microscopy is applied in a period up to 72 hours (figure 6.46). Cells correctly adhered to polystyrene surfaces, to Palamed® surfaces, as well as on P10, P15 and P20 surfaces in the first 24 hours of cultivation (Fig. 6.44 a-e) and the density increased in the following 48 (Fig. 6.44 f-l) and 72 (Fig. 6.44 m-q) hours for all samples.

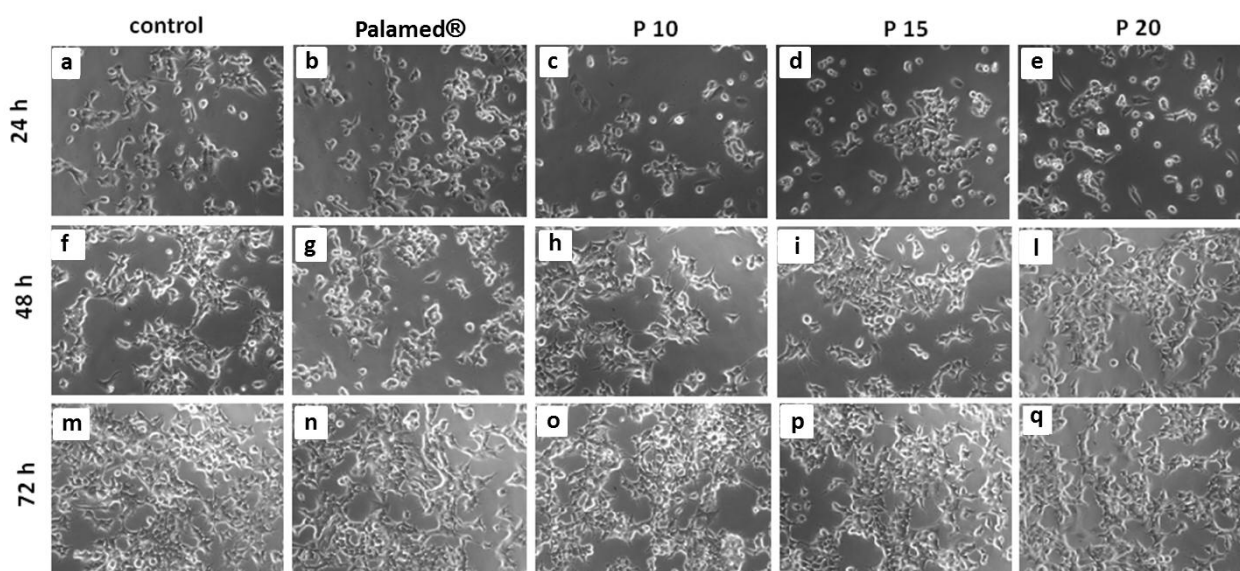


Figure 6.46: Human osteoblasts morphology, adhesion and density after 24, 48 and 72 hours of cultivation: comparison between control (polystyrene), Palamed® and composite samples (P10, P15 and P20). Bar scale=50µm.

The morphological tests are performed for each sample (Palamed®, P10, P15, P20) at three different time (24, 48, 72 hours) after cells seeding. The results are presented evaluating the cell spread on the material surface, detection of bridging connection between cells and calcium phosphate precipitates. For this test MG63 cells, a cell line coming from osteosarcoma tumor, common used for biocompatibility evaluations, are used. This cell line was selected since MG63

Results and Discussion Composite bone cement characterization

cells possess an higher capacity to proliferate respect to the non-tumoral human osteoblast and a faster response to material-cell interaction.

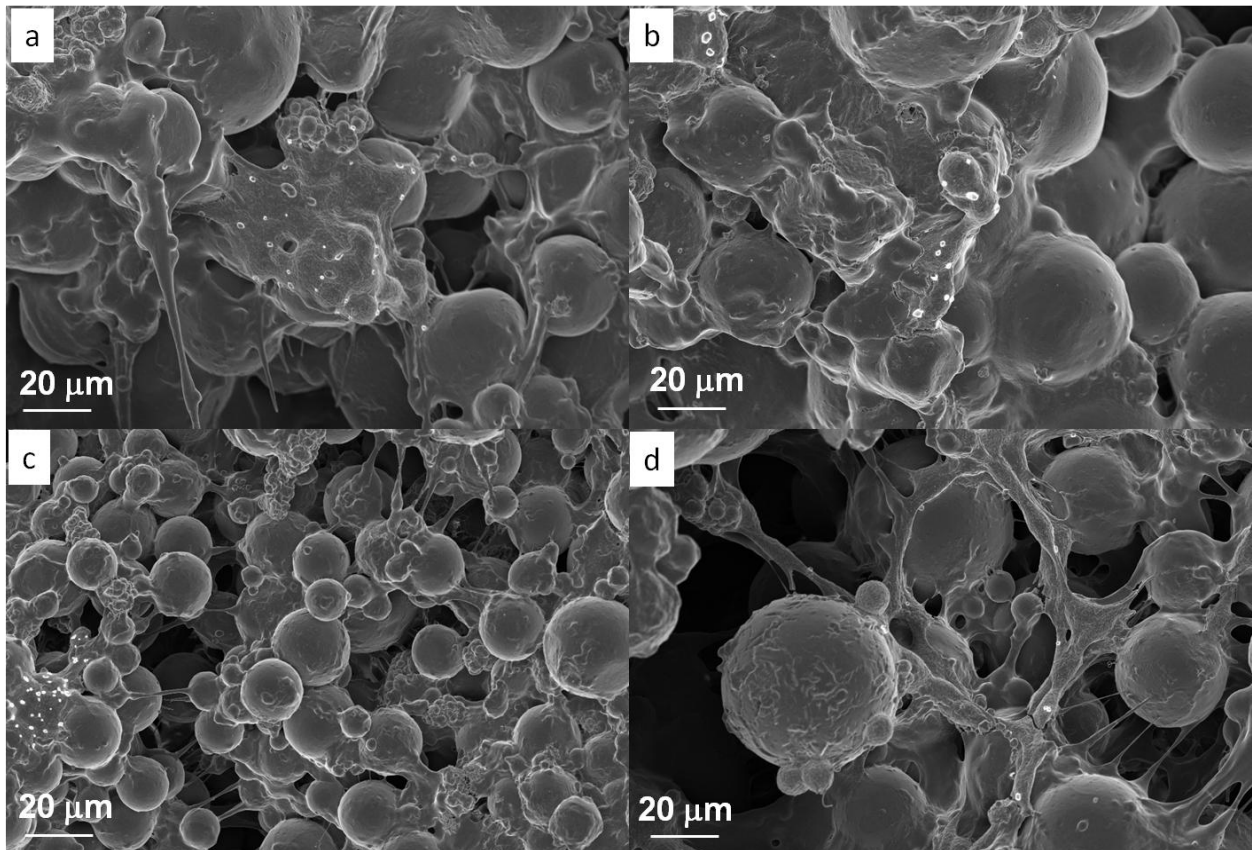


Figure 6.47: FESEM morphology of cells seeded on Palamed® after 24 hours of cultivation.

Figure 6.47 reports different morphology of Mg63 osteosarcoma cells on the surface of Palamed® cement. Different shapes of cells are observed and after 24 hours from the seeding. They well proliferate and their viability is near to 100 %. In figures 6.47a-b they appear in a compact form while in figure 6.47c-d present many connection one each other.

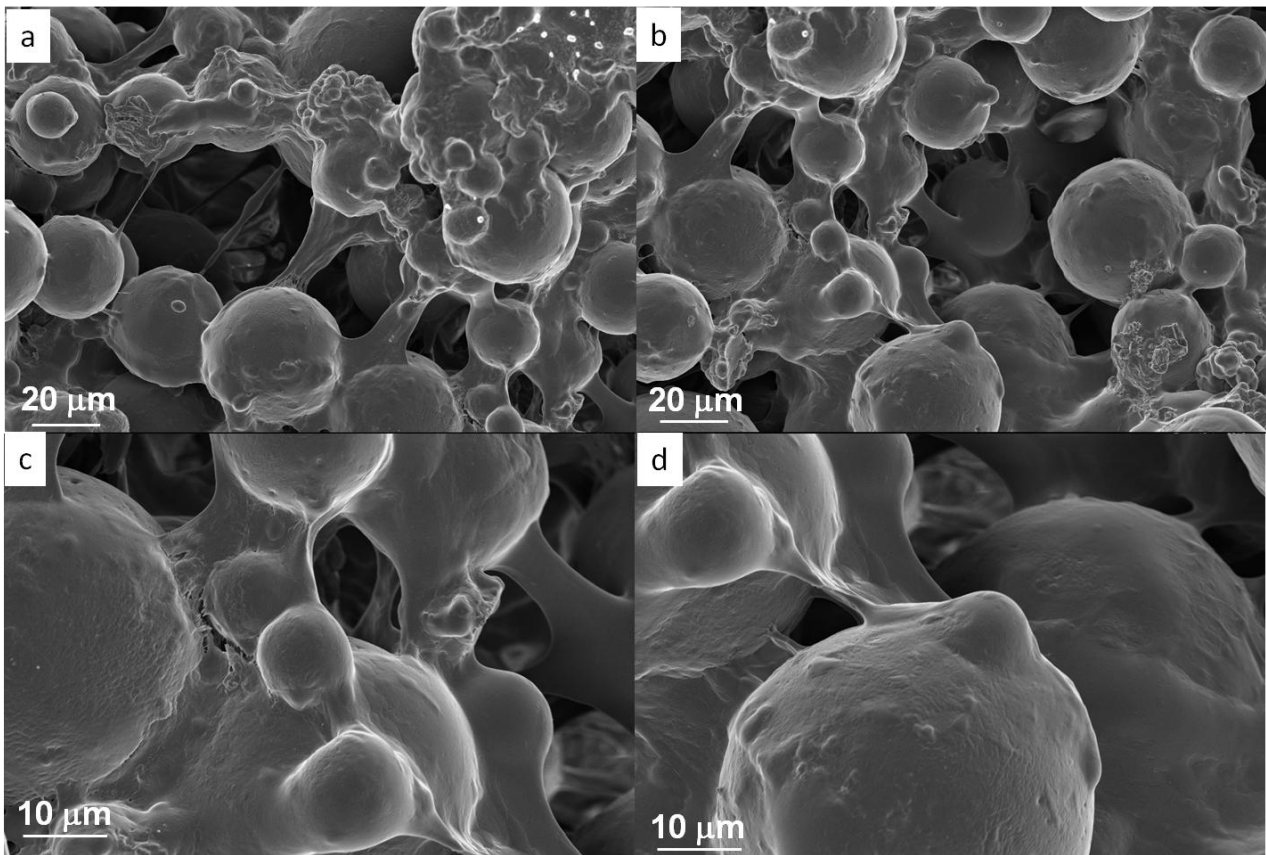


Figure 6.48: FESEM morphology of cells seeded on Palamed® after 24 hours of cultivation

Figure 6.48 reports cells adhere onto Palamed® surface showing a different morphology. In figure 6.468 they have a spherical cellular body while in figure 6.48d they possess a flat profile. The cells are spread on the cement surface, creating bridges and connection. It is impossible to distinguish one cell to other.

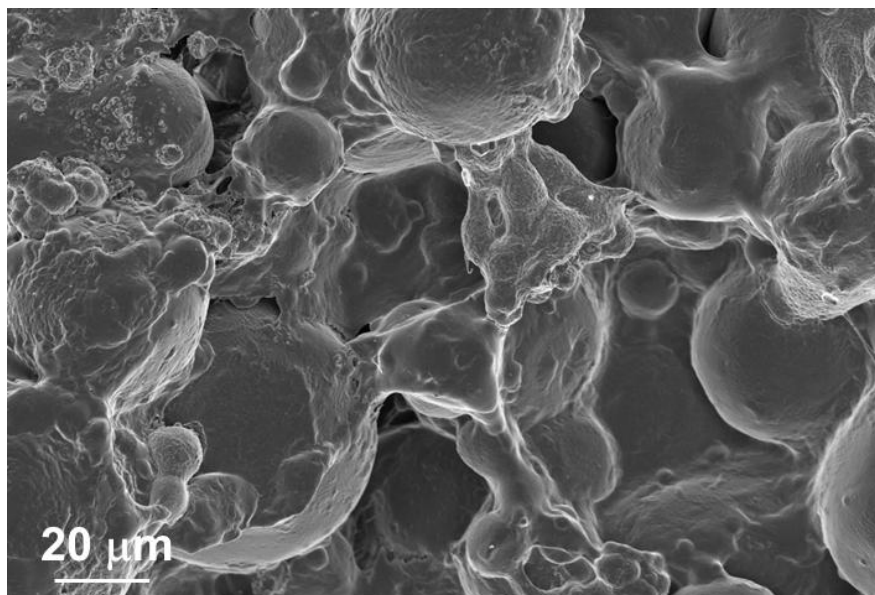


Figure 6.49: FESEM morphology of cells seeded on Palamed® after 24 hours of culture

Results and Discussion Composite bone cement characterization

Another different shape and morphology of the cells on the Palamed® are seen in figure 6.49. The cells are well spread and present an homogeneous distribution on surface.

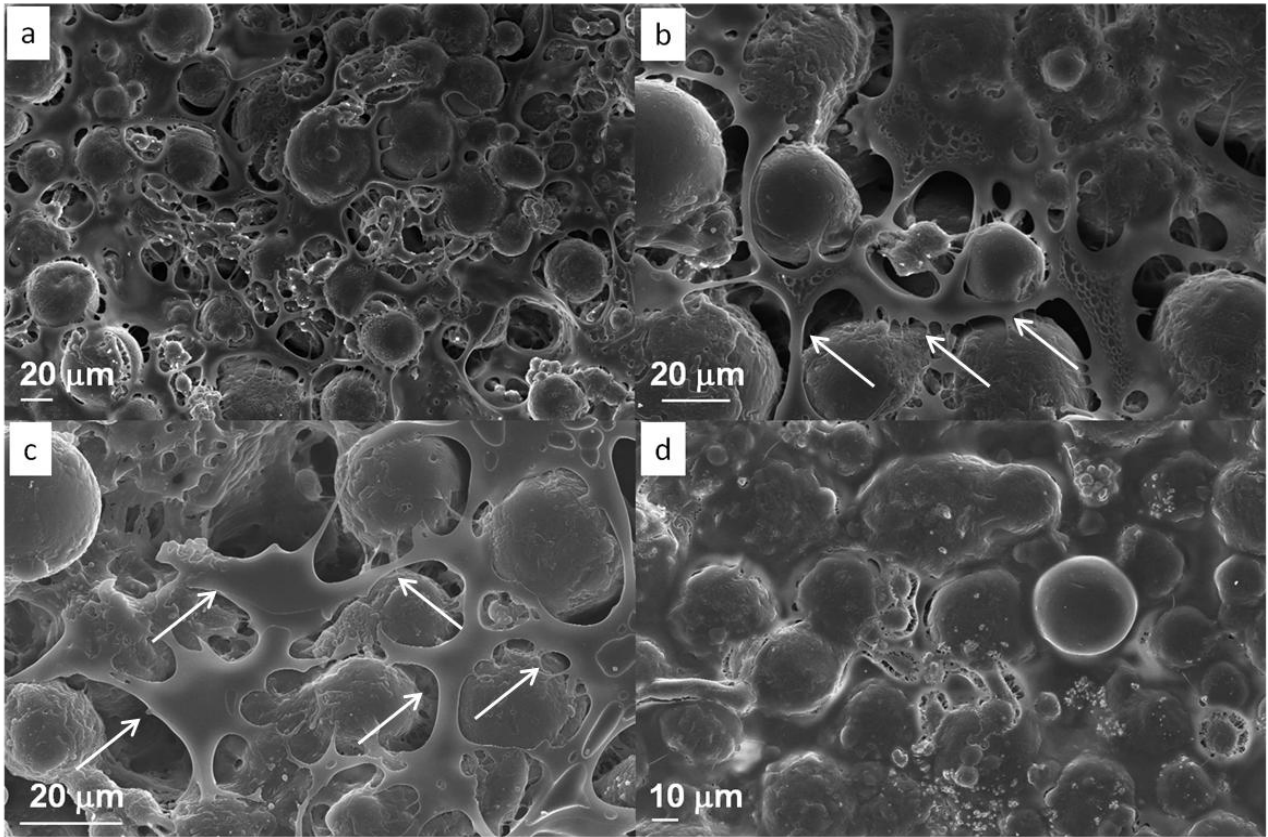


Figure 6.50: FESEM morphology of cells seeded on Palamed® after 48 hours of cultivation

Figures 6.50a-b-c-d reported a bridging connection of cells after 48 hours (see the arrows).

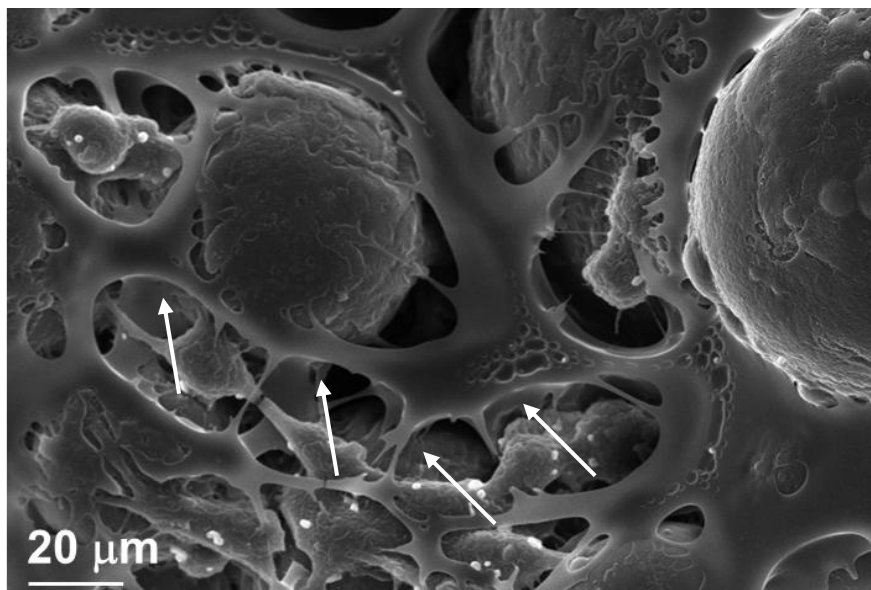


Figure 6.51: FESEM morphology of cells seeded on Palamed® after 48 hours of culture

Results and Discussion Composite bone cement characterization

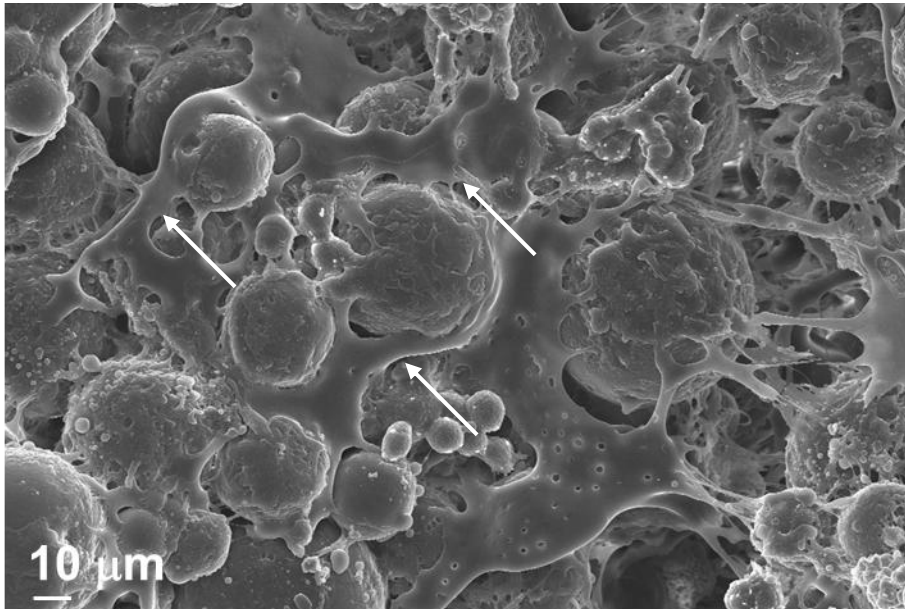


Figure 6.52: FESEM morphology of cells seeded on Palamed® after 48 hours of culture

Similar behavior was noticed in figures 6.51 and 6.52 where many cells connection are presented. The arrows in the figures show the capability of cells to develop bridging like structure.

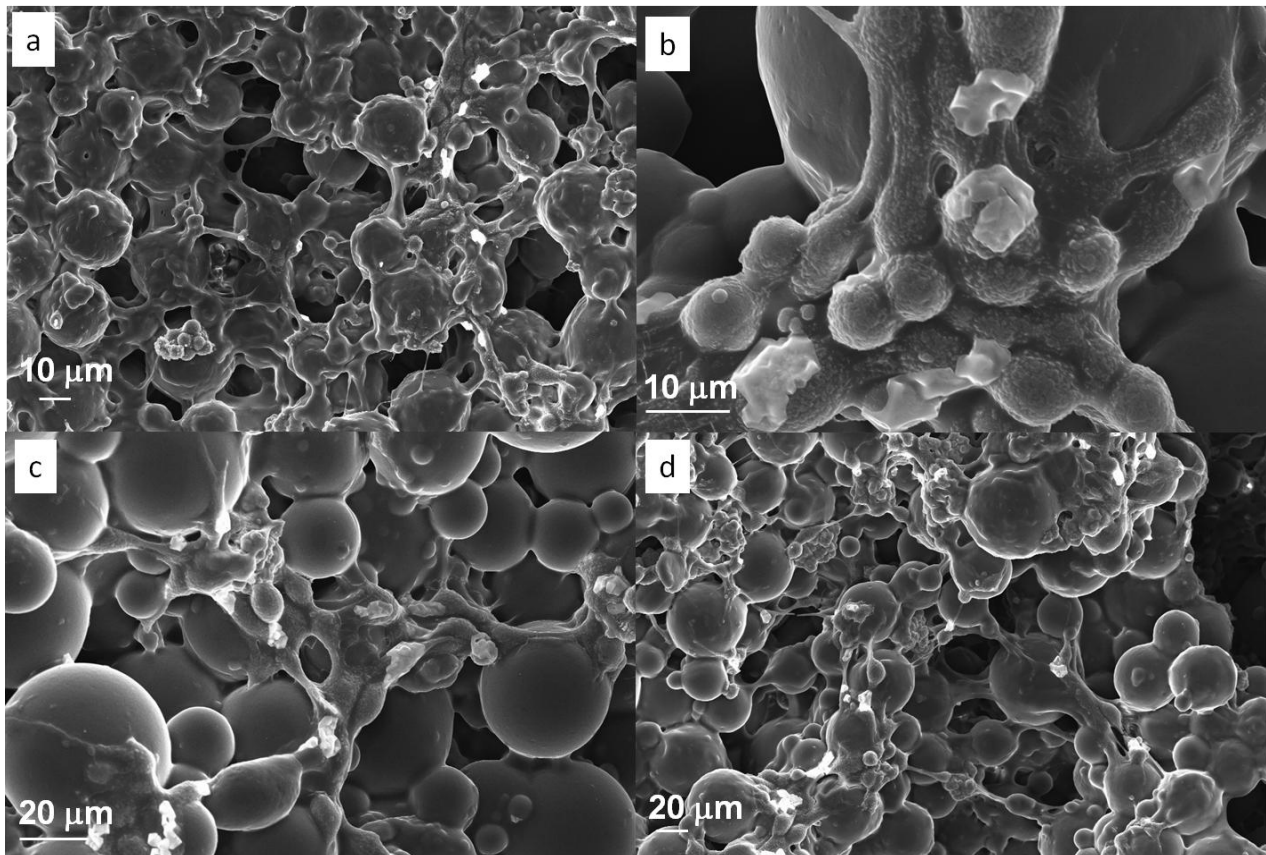


Figure 6.53: FESEM morphology of cells seeded on Palamed® after 72 hours of culture